

Effects of liquid fuel/wall interaction on thermoacoustic instabilities in swirling spray flames

E. Lo Schiavo^{a,*}, D. Laera^a, E. Riber^a, L. Gicquel^a, T. Poinso^b

^a*CERFACS, 42 avenue Gaspard Coriolis, 31057 Toulouse, France*

^b*IMFT, Allée du Professeur Camille Soula, 31400 Toulouse, France*

Abstract

Computational prediction of thermoacoustic instabilities arising in gas turbine and aero-engine combustors still remains a challenge especially if fuel is injected in a liquid spray form. This study shows that, in LES of such a combustor, the treatment of the liquid fuel film created on the walls of the injection system affects the mean flame weakly, but modifies the flame dynamics strongly. The configuration used for this work is the experimental setup SICCA-spray measured at EM2C laboratory in Paris. First steady spray flame measurements are used to validate the LES Euler-Lagrange approach. Two modelling strategies for the interaction between the liquid fuel and the injector walls are tested with a negligible impact on the flame shape and structure. In the second part the same comparison is applied to another operating condition where a self-sustained thermo-acoustic limit-cycle is experimentally observed. In that case resonant coupling is achieved with LES, confirming the adequacy of the approach but only when the film layer is taken into account. Indeed, contrarily to the stable configuration, the difference between the two Lagrangian boundary conditions is shown to have a major impact on the feedback mechanism leading to the thermoacoustic oscillation.

Keywords: Thermoacoustic instabilities, Combustion modelling, Two-phase flows, LES, Liquid/wall interaction

*Corresponding author: loschiavo@cerfacs.fr

1. Introduction

Modern gas turbines operating in lean conditions to reduce the production of pollutants, such as NOx, are known to be prone to thermoacoustic instabilities, which in extreme cases lead to fatal failure of the engine [1]. It is well known that the mechanism leading these phenomena is the closure of a feedback loop between the noise produced by the flame and the response of the flame itself to acoustic waves [1, 2]. However, the prediction of such occurrences still remains a challenge. In this specific context, many tools have been developed to investigate thermoacoustic instabilities: from analytical models or low-order models [3–5] to the more expensive Large Eddy Simulation (LES) Computational Fluid Dynamics (CFD) tool. In the last two decades, LES has been applied to study combustion dynamics of purely gaseous flames in multiple regimes [6–9] and a comprehensive review of recent progress in the field of thermoacoustic combustion instabilities in propulsion engines can be found in [10, 11] for example.

When trying to reproduce the dynamic response of real systems, and more specifically of the next generation of aero-engines, it is important to take into account the injection of liquid fuel. In terms of modelling, tackling the problem of two-phase flows is a major issue [12–14]. In the framework of thermoacoustic instabilities, a first computation of such a type was carried out by Innocenti *et al.* [15] using a Lagrangian formalism for the liquid phase coupled to the Unsteady Reynolds Averaged Simulations (URANS) to study the flame response to acoustic perturbations of a laboratory scale longitudinal aero-engine combustor. Although the trends are captured in terms of gain and phase, mismatches are present with respect to reported experimental data. A key aspect, in that case, is the capacity of properly taking into account the properties of the liquid phase and its dynamic response. Two numerical approaches can be applied to simulate the liquid phase. The first one relies on the representation of the liquid phase through an Eulerian framework [16, 17] which is straightforward in terms of computational effort but reduces drastically the possibility to account for complex properties of sprays with large polydispersity for example. Euler/Euler approach has however already been applied with LES to study thermoacoustic instabilities in real configurations with satisfactory results when it comes to the main flow properties [18]. The second approach is to adopt the Lagrangian framework which solves the trajectory for each particle introducing difficulties such as load balancing because of the particles motion in the gaseous field [19] and

their non-uniform distribution in the computational domain or the treatment when reaching the boundaries. Recently this approach has been applied to many realistic LES applications with multiple aims like ignition [20] or stabilized flames [14] as well as thermoacoustic instabilities [21]. In this case, correctly reproducing the liquid droplet behavior is a key aspect, since the feedback loop between the acoustic field and the flame is coupled to the particle dynamics [22, 23]. Recent studies have been performed to better understand this mechanism. For example Kitano *et al.* [24] studied particle dynamics during a thermoacoustic oscillation for a laboratory step configuration linking the intensity of the thermoacoustic oscillation amplitude to the injected particle diameter, emphasizing how phase change in the evaporation rate induced by the droplet size could impact the instability. The academic test-case of a back-step flame was later studied by Tachibana *et al.* [21] as a realistic aero-engine experimental setup, showing again the importance of the fuel released by evaporation in the combustion chamber with a direct effect on the evaporation rate fluctuations feeding the heat-release rate and therefore driving the instability. However, results only looked qualitatively satisfactory and the study showed quantitative discrepancies in fluctuation amplitude and local flame behavior in part because of the complexity of the geometry or errors in measurements. Note that for all above mentioned studies the interaction between liquid particles and walls are always simplified. The present work wants to show the importance of this feature in laboratory-scale applications aiming to reproduce the physics of real combustion chambers. Indeed, in many aero-engine airblast atomizers [25], the liquid fuel is injected at high pressure on a metal surface called prefilmer with the aim of better atomizing the liquid fuel coming from the pressurized tank [26]. The importance of correctly modelling this film to reproduce thermoacoustic oscillations in real configurations needs to be evaluated. The physics of this process is however quite complex given the current incapacity to experimentally visualize these regions in real applications or in experimental setups with or without thermoacoustic instabilities.

This document is divided in four parts. First, in Sect. 2, the LES numerical methodology and the SICCA-spray configuration of EM2C are described. Then, in Sect. 3.1, the cold flow is validated by comparison with measurements while in Sect. 3.2 the steady flame results are analyzed with a first sensitivity analysis to the treatment of the droplets boundary condition on the injector wall. Finally, in Sect. 3.3, the dynamic response of the flame is investigated in the self-excited limit-cycle condition of the SICCA-

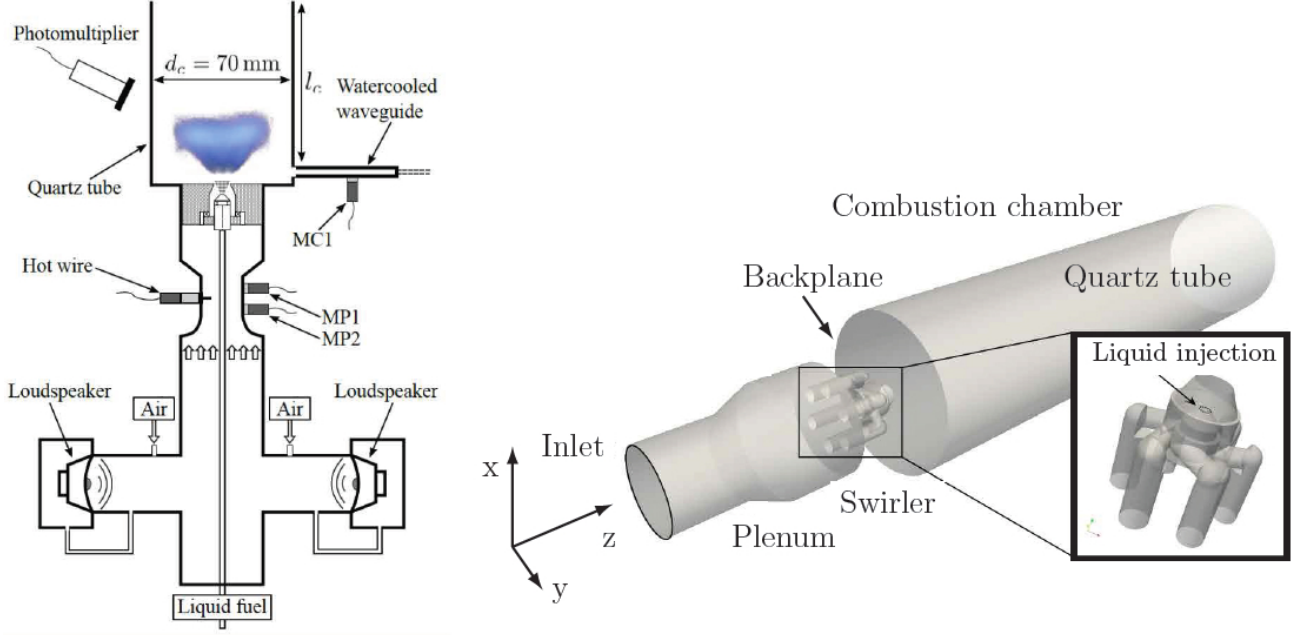


Figure 1: SICCA-spray: experimental setup [29] (left) and numerical setup (right).

spray [27, 28].

2. Numerical setup and Modeling

The SICCA-spray experimental setup, sketched in Fig. 1(left), is a single burner swirled spray n-heptane/air flame configuration [29]. It is a longitudinal setup where air flows from a plenum into a cylindrical combustion chamber equipped with a radial swirler. A typical hollow-cone shape atomizer enables liquid fuel injection on the centerline of the swirler. Note that LDV measurements of the gaseous velocity profiles in cold conditions are performed without confinement to avoid laser beam deflections due to wall wetting [30]. Moreover, the feedback loop between the flame and acoustics closes only when the chamber is longer than a threshold value [27]. To experience the self-sustained limit-cycle the quartz tube length was adapted to trigger this thermoacoustic oscillation modifying the first longitudinal mode of the chamber. For these reasons three different computational domains are used to mimic the three experiments operating with the same air mass flow rate, $\dot{m}_{air} = 2.58$ g/s, and global equivalence ratio, $\varphi = 0.85$, for the

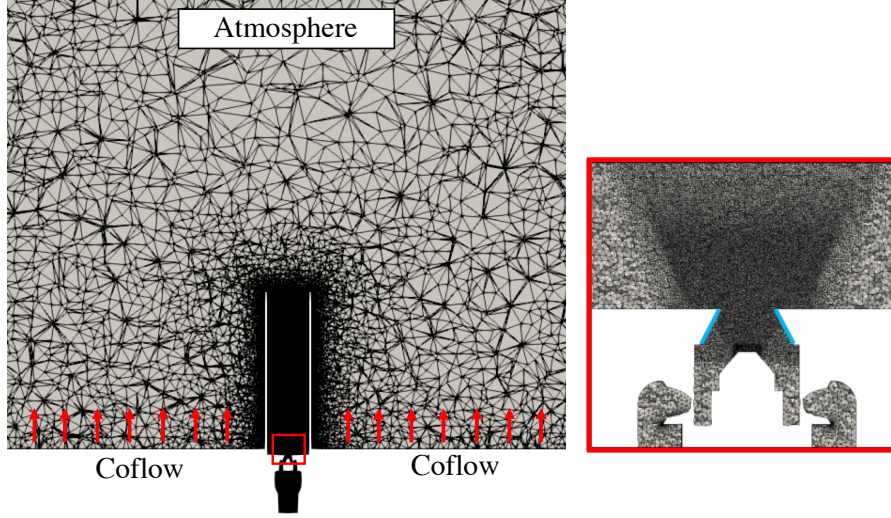


Figure 2: The meshed numerical domain comprising the SICCA-spray and the atmosphere. In the zoom window, the injector walls where the spray impacts before entering the combustion chamber are highlighted in blue.

reactive cases:

- The cold case with an unconfined domain.
- The stable condition with $\ell_c = 165$ mm and for which the flame does not present thermoacoustic oscillations.
- The limit-cycle condition with $\ell_c = 280$ mm where the system resonates with a thermoacoustic mode.

Except for these geometrical changes, stable and unstable flames present the same operating condition, mesh refinement and modelling as detailed hereafter. The computational domain is discretized with a 20 million cells mesh shown in Fig. 2. The finest mesh zone is located at the injector exit so that the reactive simulations correctly reproduce the flame root dynamics (zoom window in Fig. 2). In that case, the stoichiometric n-heptane laminar flame thickness ($\delta_l = 410 \mu\text{m}$) can be used suggesting $\Delta x \simeq 150 \mu\text{m}$. Larger cell sizes around $\Delta x \simeq 200 - 300 \mu\text{m}$ are used further downstream near the combustion chamber exit and in the injector zone while $\Delta x \simeq 500 \mu\text{m}$ in the swirler core.

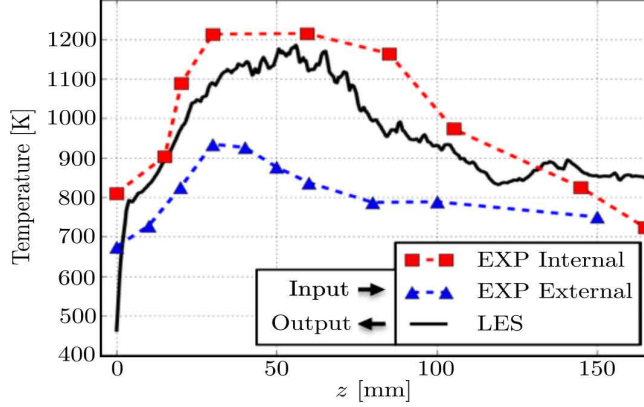


Figure 3: Temperature axial profile on the combustion chamber wall in steady conditions. Comparison between external measurement (blue triangle), internal measurement (red square) and LES results (black solid line).

2.1. Gaseous phase modelling

The computational domain, Fig. 1(right), includes the atmosphere to correctly reproduce the acoustic boundary condition at the combustion chamber outlet. To ease the flow establishment in this outer region a slow co-flow is introduced, as shown in Fig. 2, to simulate the entrainment of the air by the combustor. The LES main flow inlet is in the plenum at the same location of the hot wire in the experiment (MC1 location on Fig. 1(left)).

The simulations are performed using the code AVBP developed by CERFACS (<http://www.cerfacs.fr/avbp7x>). The fully compressible LES-filtered Navier-Stokes equations, enlisted in details in [4], are solved using a third-order accurate in time and space Taylor-Galerkin scheme [31]. The Navier-Stokes Characteristic Boundary Conditions [32] are also used to treat the inlets and outlets of the simulations. According to theory [33], the inlet reflection coefficient is affected by the relaxation coefficient K as a function of frequency $\omega = 2\pi f$ for both magnitude and phase: $||R|| = 1/\sqrt{1 + (2\omega/K)^2}$ and $\varphi = -\pi - \arctan(2\omega K)$. For the steady flame calculations $K_{st} \simeq 1000 \text{ s}^{-1}$ is used. In the limit cycle case, starting from this value, K is reduced until a resonant condition is achieved for $K_{lc} \simeq 10 \text{ s}^{-1}$, which was verified to be still sufficient to avoid any mean value drift. The mass flow rate, \dot{m}_{air} , is fixed at the plenum with a turbulent mean profile, whereas for the co-flow a constant velocity of $w_{cofl} = 0.3 \text{ m/s}$ is imposed. For the atmospheric outlet, ambient pressure is imposed ($p = 101325 \text{ Pa}$ with $K_{out} = 10 \text{ s}^{-1}$).

Walls are considered as no-slip and adiabatic except for the backplane and the combustion chamber wall, where heat losses are not negligible in hot conditions [27]. In this case, the metal backplane of the combustion chamber is considered to be at a constant temperature of $T_{bkpl} = 450$ K and a small heat resistance of $R_{bkpl}^h = 1 \cdot 10^{-4}$ m²K/W is used to allow for heat to flow away from the surface. Regarding the combustion chamber wall, an axial temperature profile is imposed using the experimental data measured on the external side of the combustion chamber. Imposing the correct value for the heat resistance based on the quartz thermal conductivity and the quartz width ($R_{chwl}^h = 1.38 \cdot 10^{-3}$ m² K/W), the temperature value on the inner wall becomes an output of the simulation, as verified in Fig. 3, which shows agreement with internal measurements [27].

For all simulations, the turbulence subgrid model is WALE [34] and chemical reaction is described with the global two-step scheme *2S_C7H16_DP* involving 6 species and 2 reactions with pre-exponential adjustment (PEA) upon local equivalence ratio to correctly reproduce the laminar flame speed for rich mixtures [35]. For the present conditions, the premixed flame thickness is $\delta_L = 410$ μ m, suggesting that with the mesh refinement in flame region used here a subgrid scale combustion model is needed. Whenever a reactive zone is detected by a flame sensor, the classical dynamic TFLES [36] model is employed coupled with the efficiency function proposed by Charlette *et al.* [37]. Although this model has long been validated in multiple configurations a particular attention in a liquid fuel combustor is required. Indeed, as shown in a recent study by Rochette *et al.* [38], evaporation driven spray flames result in thicker reaction zones compared to their respective gaseous flames operating at the same equivalence ratio. Moreover, the combustion regime of two-phase flames is yet not well distinguished from the premixed and non-premixed conditions meaning that the application of a standard dynamic thickening factor affects the partially premixed or even diffusion flame. Here, the Takeno index [39], $TKN = \nabla Y_{C_7H_{16}} \cdot \nabla Y_{O_2} / |\nabla Y_{C_7H_{16}} \cdot \nabla Y_{O_2}|$ is used to locally detect the premixed flame regions and apply a local thickening depending both on equivalence ratio and local resolution. Thickening is deactivated in diffusive flame regions, the TFLES formalism and the efficiency functions being formally applicable only to premixed flames [40]. The terms coupling the liquid and gaseous phases are a direct consequence of the heat released by the flame, therefore, according to the TP-TFLES model [41], when thickening the flame with a turbulent combustion model the coupling terms (evaporation and drag) between the two phases need to be divided by

the same thickening factor used by the TFLES model to preserve constant the ratios between the droplet relaxation timescale, the evaporation timescale and the chemical timescale as in the non-thickened flame.

2.2. Liquid phase modelling

A Lagrangian formalism is adopted to model the liquid spray. Droplet evolution forces are obtained using the Schiller-Neumann correlation for the droplet drag coefficient [42] while evaporation is modeled according to Abramzon and Sirignano [43]. The Prandtl and Schmidt numbers for the liquid phase are $Pr^{ev} = 0.976$ and $Sc^{ev} = 1.343$ for the evaporation process as in [44]. Two way coupling is considered for the liquid-gas interaction by use of a first order interpolation. The time integration for particle trajectory is obtained using two-step Runge-Kutta scheme so that $\Delta t_p = 2\Delta t$. The liquid particles are considered as much smaller than the LES grid size and their deformation is negligible. Likewise gravity and shear effects are supposed negligible compared to drag. The detailed formulation of the source terms used to solve the LES equations for the liquid-gas phase coupling is reported in 4 together with the closure terms for the droplet evaporation and heat flux.

Addressing numerically liquid injection into the combustion chamber, and capturing the specific liquid phase physics, is an open challenge. Hereafter, the main characteristics of this physical phenomenon are summarized and sketched in Fig. 4:

1. *Primary atomization:*

In the atomizer the liquid is injected through a high-pressure channel and swirled. A film region is shaped as a hollow cone which creates ligaments and big droplets because of high shear conditions.

2. *Secondary breakup:*

The liquid, subject to the aerodynamic field, is either further split into smaller droplets and/or coalescence occurs between very small droplets.

3. *Splash:*

When a liquid spray impacts a wall, multiple complex interactions may occur [45]. The particle properties, such as their size, temperature and momentum strongly affect this phenomenon. The characteristics of the surface, especially its temperature, roughness, wettability or the presence of a film layer [46, 47] are also of importance in that case.

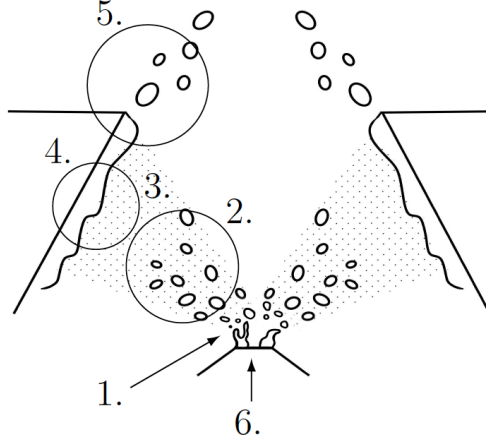


Figure 4: Sketch of the interaction between spray and turbulence before entering the combustion chamber.

4. *Liquid-wall interaction:*

The liquid impacting the wall then forms a film which slides on the injector wall until it reaches the combustion chamber where it is released.

5. *Edge atomization:*

At the edge of the injector, liquid fragmentation occurs because of transverse instabilities in the flow.

6. *Unsteady injection model:*

In the context of thermoacoustic instabilities, the resonant coupling between pressure and heat release may be linked to fluctuations of the injected fuel mass flow rate [1]. The inclusion of this instability driving mechanism requires the definition of an unsteady injection model.

In this work primary (1.) and secondary (2.) atomization phenomena are not explicitly simulated but the semi-empirical model FIM-UR [48] is used to prescribe a droplet diameter distribution at the atomizer orifice that enables to correctly reproduce the spray velocity and diameter distribution downstream the atomization process when the spray is diluted [44].

The atomizer parameters used in the experiment are the diameter of the discharge orifice $D_0 = 120 \mu\text{m}$ and the fuel line $\Delta p \simeq 9 \text{ bar}$, translating in $\theta = 45^\circ$ for the injection model. Droplets are assumed to be at $T_{fuel} = 300 \text{ K}$ and a *Rosin-Rammler* probability function fitted on mean and Sauter diameters $D_{10} = 10 \mu\text{m}$ and $D_{32} = 18 \mu\text{m}$ respectively. These values are extracted from measurements at $z = 2.5 \text{ mm}$ from the chamber backplane [30]. The

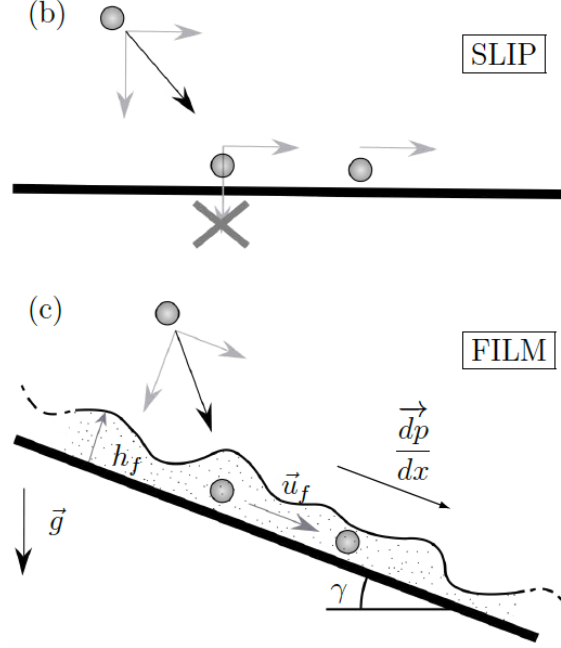


Figure 5: Sketch of the two treatments for the liquid-wall interaction. (a) Slip condition: particles move independently on the wall (b). Film condition: the film velocity is the same for the whole set of particles moving on the wet surface.

distribution being known in the simulation and fixed, the changes of diameter due to splash (3.), edge atomization (5.), primary (1.) and secondary (2.) atomization are not explicitly simulated, as in [14] for example.

Notice that the assumption of a constant value for both the cone angle and the liquid mass flow rate may not be justified when thermoacoustic oscillations occur. However, the impact of thermoacoustic oscillations (6.) on the injection system itself can be neglected since the Δp of the atomizer is approximately one order of magnitude higher than the measured thermoacoustic oscillations ($p' \simeq 1 - 2$ kPa) so a constant liquid fuel mass flow rate, $\dot{m}_{fuel} = 0.144$ g/s, imposed.

The present work focuses on the liquid-wall interaction (4.) and the numerical treatment of the film. Two particle-wall interaction treatments (summarized in Tab. 1) are tested and their impact on the spray-flame stabilization and the thermoacoustic combustion instabilities is evaluated:

- A “slip condition” [50] for which the wall normal velocity of the droplet is set to zero. As shown in Fig. 5 (a), droplets then stick to the wall

Treatment	Characteristics
Slip	Particles reaching the walls slip along the wall at their initial speed
Film	Particles reaching the wall form a film. Its depth and speed are calculated using St. Venant equations [49]

Table 1: Wall treatments for the liquid fuel phase

and their inertia moves each particle independently due to the local flow velocity.

- A “film condition” that accumulates the droplet in a Lagrangian liquid film layer whose depth and velocity are evaluated using Saint-Venant equations [49] as proposed in [51] and further developed in [?]. In that case, Fig. 5 (b), droplets are trapped by the film layer and start moving with a locally averaged velocity which corresponds to the film velocity and depends on the local shear stress and film height as well as the local volume of particles contained in the boundary cells where the model is activated. Particles are then released by the liquid sheet when an edge with angle higher than 60° is encountered. A first application of this modelling in a configuration featuring an airblast atomizer can be found in Ref. [53]

Note that the two cases will be now referred to as SLIP and FILM, respectively. The choice of this film boundary condition in the context of this study is supported by early experimental visualizations in the SICCA-spray chamber suggesting that the majority of the liquid fuel enters the combustion chamber after interacting with the injector walls (e.g., see Fig. 2 in [30]). Unfortunately, since the particle-wall interactions mainly happen inside the injector, no further experimental data is available leaving the validation of these suggestions to high-fidelity numerical simulations.

Film modelling is briefly recalled hereafter. More details can be found in Ref. [?]. Starting from the incompressible formulation, Navier-Stokes equations for the film layer equations read

$$\nabla \cdot \mathbf{u} = 0 \quad , \quad \frac{D\mathbf{u}}{Dt} = -\frac{1}{\rho}\nabla p + \nu\nabla^2\mathbf{u} + \mathbf{g}. \quad (1)$$

Non-dimensional analysis and steady state assumptions for a 2D liquid sheet produce

$$\left\{ \begin{array}{l} \frac{dv}{dy} = 0 \\ v \frac{du}{dy} = -\frac{1}{\rho} \frac{dp}{dx} + \nu \frac{d^2u}{dy^2} + g \sin \gamma \\ \frac{dp}{dy} = 0 \end{array} \right. \quad \text{with} \quad \left\{ \begin{array}{ll} \mu \frac{\partial u}{\partial y} = \tau_w & y = h(x, t) \\ u = 0 & y = 0 \\ v = 0 & y = 0 \end{array} \right. \quad (2)$$

which together with closure at the film boundaries, $v = 0$ and $p = p_{ext}(x)$, leads finally to

$$\nu \frac{d^2u}{dy^2} = \frac{1}{\rho} \frac{dp}{dx} - g \sin \gamma \quad \text{with} \quad \left\{ \begin{array}{ll} \mu \frac{\partial u}{\partial y} = \tau_w & y=h(x, t) \\ u = 0 & y=0 \end{array} \right. \quad (3)$$

Once integrated the expression of u along the film thickness reads

$$u(y) = \left[\left(\frac{dp}{dx} - \rho g \sin \gamma \right) \left(\frac{y}{2} - h \right) + \tau_w \right] \frac{y}{\mu}. \quad (4)$$

Averaging the liquid velocity along its depth, and thus assuming locally the same velocity component for the whole set of particles contained in a boundary cell, one gets,

$$\bar{u}_f = \frac{1}{h} \int_0^h u(y) dy = \tau_w \frac{h}{2\mu} + \left(\rho g \sin \gamma - \frac{dp}{dx} \right) \frac{h^2}{3\mu}. \quad (5)$$

To better understand the physics behind the model, a first order expansion of the film thickness h without gravity or pressure gradient can be useful to recover a characteristic film velocity noted $U_{f,0}$ scaling and which follows

$$U_{f,0} \sim \tau_{w,0} \frac{h_0}{\mu_0}. \quad (6)$$

3. Results and discussion

In the first part of the following discussion the cold flow is analyzed. In the second part the steady-state reacting conditions are examined. The effect of the treatment adopted for the liquid impinging the wall in the steady reactive case and with thermoacoustic instabilities will be presented and discussed in Sect. 3.2 and Sect. 3.3, respectively.

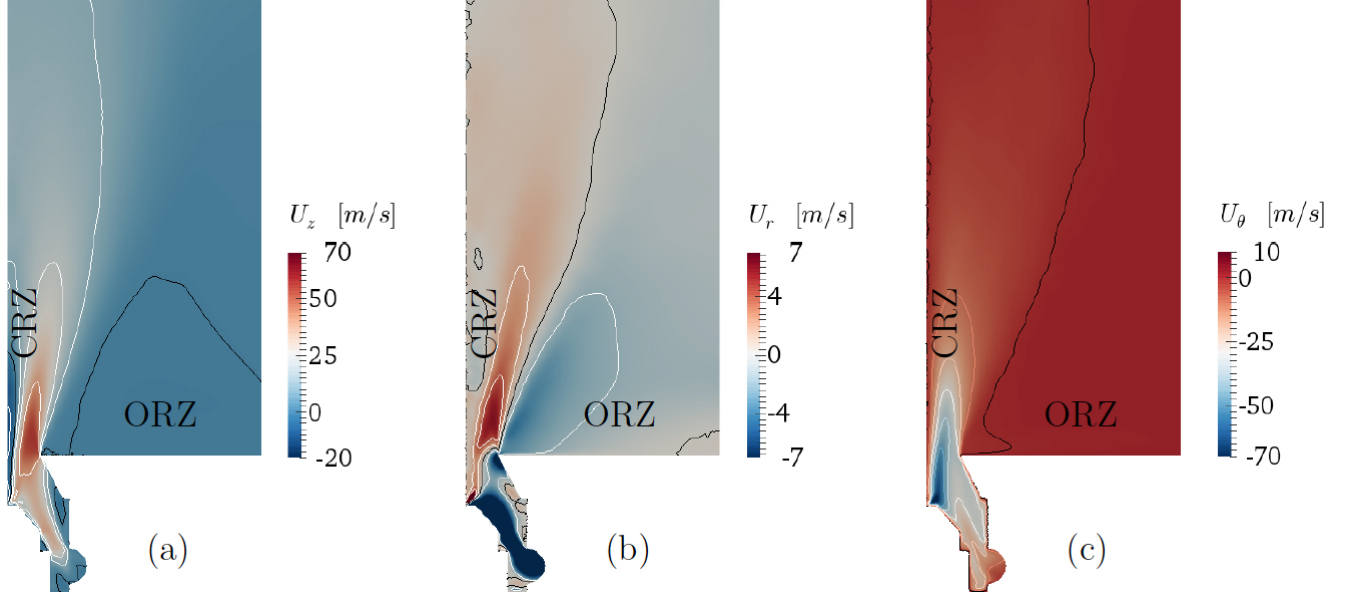


Figure 6: Axial, radial and tangential velocity components respectively U_z , U_r and U_θ ; time and angle average contours. (black line is $U_z = 0$, $U_r = 0$, $U_\theta = -1$).

3.1. Cold flow conditions

Cold flow predictions are first addressed. To do so, for the purely gaseous jet, time ($t_{av} = 15$ ms) and angle average contours of axial, radial and tangential velocity components are respectively reported in Fig. 6. Figure 6 (a) shows that the swirled jet is characterized by a strong central recirculating zone (CRZ) and an outer recirculating zone (ORZ) limited by the black isoline indicating the zero streamwise velocity. The jet opening is visualized from Fig. 6 (b) by the ORZ where the radial velocity pushes the cold gases in the corner through the jet axis. Figure 6 (c) visualizes the jet by showing the tangential velocity component. The validation of the gas phase is presented in Fig. 7 by comparing the jet mean and root-mean-square (rms) velocity profiles for the numerical prediction and the experiment taken at three planes located at $z = 2.5, 5$ & 10 mm from the combustion chamber backplane. The mean axial velocity peak as well as the intensity of the CRZ are well captured by LES (Fig. 7 (a)left) in the three planes. A mismatch is observed on the peak position of the radial velocity component (Fig. 7 (b)left) leading to an underestimation of the jet opening angle. Finally, the tangential component, Fig. 7 (c)left, does show good agreement with the experimental values.

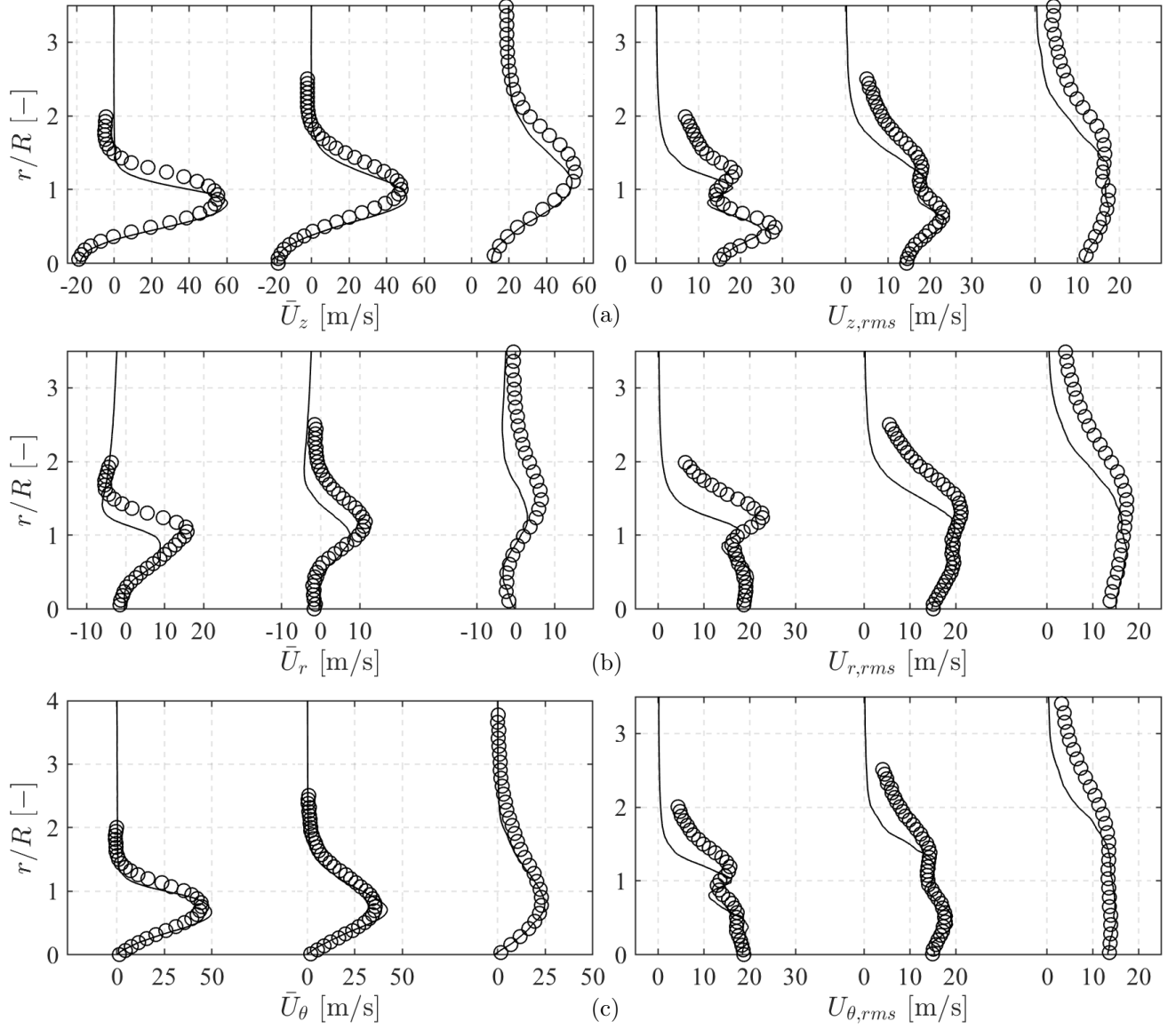


Figure 7: Comparison between experiments [27] (symbols) and LES (solid line) at $z = 2.5, 5 \text{ \& } 10$ mm from the chamber backplane for the mean velocity profiles (left) and rms (right). Axial (a), radial (b) and tangential (c) components respectively. The radial coordinate r is reported normalized with respect to the radius of the injector exiting section $R = 4$ mm.

Fluctuations of the three velocity components, Figs. 7 (a-c)right, are well captured in the central part of the jet ($r/R < 1$). On the contrary, probably

due to the jet opening underestimation, LES slightly underpredicts velocity oscillations in the external part of the jet ($r/R > 1$). Overall, global quantities such as the swirl number of the jet and the injector head loss (reported in Tab. 2) are in good agreement with the experimentally reported values confirming the appropriateness of the adopted mesh refinement.

	Equation	Experiment [27]	LES	Error
Head loss	$\Delta p = p_{max}^{pl} - p_{max}^{ch}$	3900 Pa	4092 Pa	5 %
Swirl number	$S = \frac{\int_0^R 2\pi\rho U_z U_\theta r^2 dr}{R \int_0^R 2\pi\rho U^2 r dr}$	0.55	0.51	7 %

Table 2: Global quantities of the cold flow, comparison between LES and experiments

3.2. Steady flame conditions

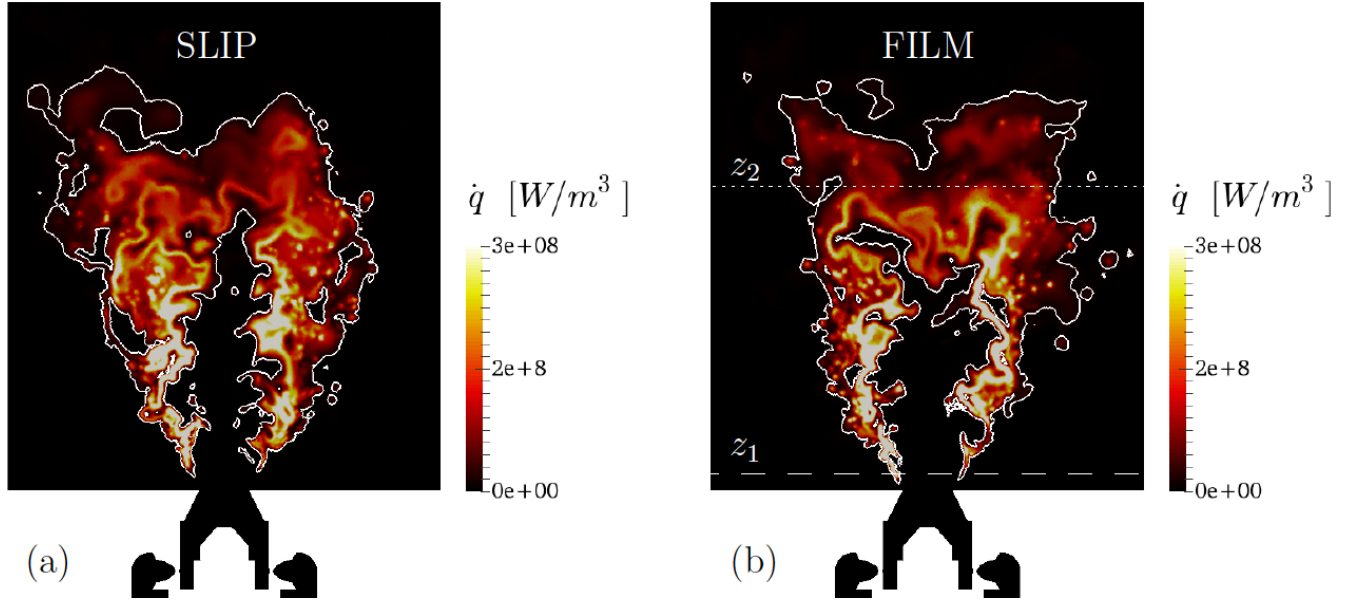


Figure 8: Instantaneous flame shape in a y-normal plane: Heat release rate for cases SLIP (a) and FILM (b). The external contour of heat releases rate is $\dot{q} = 10 \text{ MW/m}^3$. In (b) $z_1 = 2.5 \text{ mm}$ and $z_2 = 50 \text{ mm}$ are indicated.

Figure 8 shows the instantaneous flame shapes obtained with the two treatments (Tab. 1). Very similar characteristics are shown suggesting a small impact on the mean flame topology of the wall-particle interaction modelling. In Fig. 9, the complexity of this two-phase flame is emphasized by showing

the contour of the Takeno index and total equivalence ratio $\phi_{tot} = \phi + \phi_\ell$ where ϕ and ϕ_ℓ the gaseous and liquid equivalence ratios respectively, with $\phi = sY_{C_7H_{16}}/Y_{O_2}$ where $s = 3.52$ is the stoichiometric ratio and $\phi_\ell = s\alpha_\ell/Y_{O_2}$, α_ℓ being the liquid volume fraction. For both cases, the flame root presents both premixed and diffusion regimes as expected when the evaporation is the leading process [38]. Moving downstream, the premixed regime starts dominating in the center of the swirled jet where fuel vapor is trapped by the CRZ. On the external side of the hollow cone spray, combustion proceeds mainly in a diffusion regime due to the presence in that region of larger droplets and lower gas temperature induced by the ORZ.

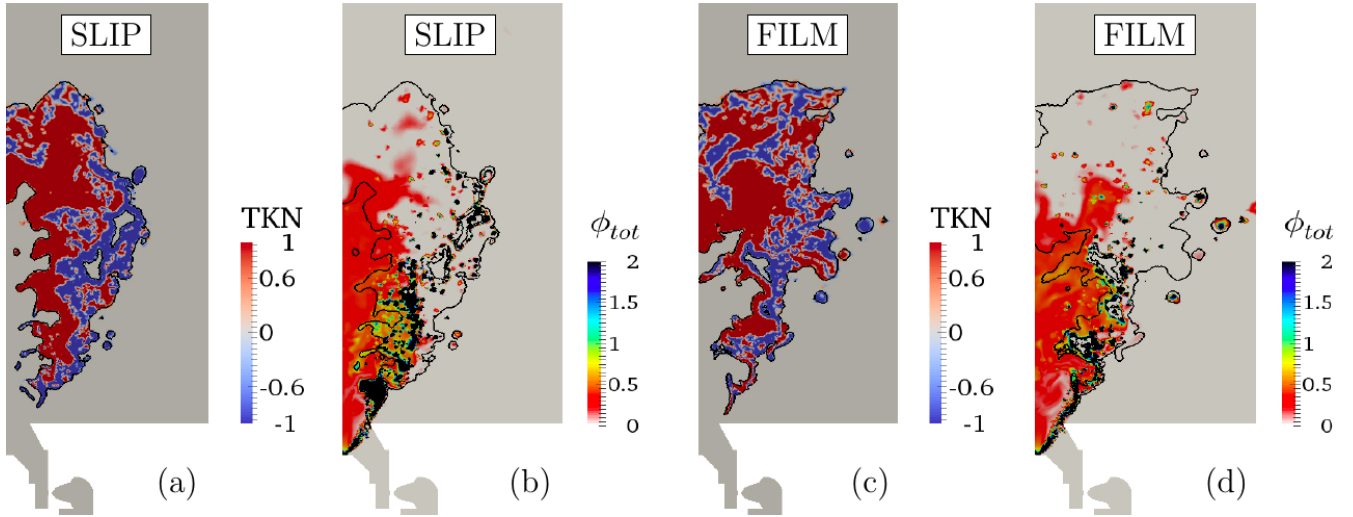


Figure 9: Y-normal plane: Takeno index in the flame region for the SLIP (a) and FILM (c) cases. Total equivalence ratio ϕ_{tot} for SLIP (b) and FILM (d) cases. The external contour of heat releases rate is $\dot{q} = 10 \text{ MW/m}^3$.

$d_p [\mu\text{m}] \setminus T [\text{K}]$	500	750	1000	1250	1500	1750
5	0.23	0.12	0.08	0.06	0.05	0.04
10	0.94	0.47	0.32	0.25	0.2	0.17
20	3.74	1.88	1.29	1	0.81	0.69

Table 3: Evaporation time t_{ev} [ms] for n-heptane droplets at $T_p = 300 \text{ K}$ and ambient pressure.

Table 3 displays the evaporation times for different gas temperatures and droplet diameters. Because of the high volatility of n-heptane, the liquid

phase evaporation times are very small as long as the particle diameter remains small. However, for particles with diameters larger than $d_p = 10 \mu\text{m}$ (e.g, see the last line in Tab. 3) the evaporation time t_{ev} and the convective time $t_w = 1.52 \text{ ms}$ needed to reach $z = 50 \text{ mm}$, evaluated using the bulk velocity at the combustion chamber entrance $U_b \simeq 40 \text{ m/s}$, become comparable. This confirms that large droplets can reach the flame tip, following the hollow cone trajectory, as visible from the spots at high ϕ_{tot} in Fig. 9. Note that such large droplets crossing the flame should burn in an isolated droplet combustion regime for which a specific model should be introduced. However, the number of these particles remains negligible and the introduction of such a model is avoided in the simulation.

Figure 10 displays a scatter plot of gas temperature versus mixture fraction $Z = \frac{sY_{C_7H_{16}} - Y_{O_2} + Y_{O_2}^0}{sY_{C_7H_{16}}^0 + Y_{O_2}^0}$ for both cases. For this diagnostic, the whole instantaneous flame is taken into account, that is to say all points inside the white contour of Fig. 8 are considered. For both cases the flame structure is very similar, the flame being mostly burning in a premixed regime (red scatter) following the adiabatic flamelet until the lean combustion limit is reached and the temperature decreases drastically ($Z \simeq 0.04 \rightarrow \phi \simeq 0.6$). As expected, the flame in the non-premixed regime burns mainly at stoichiometry while the low temperature points of this combustion regime are probably linked to the two-phase flame which broadens the presence of such a front via evaporation.

Angle and time-average ($t_{av} = 30 \text{ ms}$) fields of heat release rate are then compared to experimental Abel transforms of CH^* chemiluminescence [27] in Fig. 11. Fairly satisfactory agreement in terms of flame shape and spatial distribution of the flame intensity is found for both cases. Nevertheless, a mismatch is observable in terms of heat release distribution. Indeed, in the experiment along the flame axis a secondary heat release branch typical of a M-shape flame is potentially present whereas LES predicts a classic tulip-shape flame. Since this flame is seen to be completely piloted by the evaporation of the spray, unless further information about its characteristics is available, improvement seems difficult to obtain. Moreover, a slight underestimation of the flame opening is also visible reflecting the previously discussed error in the prediction of the radial velocity component.

Figure 12 shows the axial velocity profiles at $z = 2.5 \text{ mm}$ of the fuel particles grouped in four ranges of size. The dashed line represents the mean gaseous velocity at this same location. Regardless of the wall-interaction

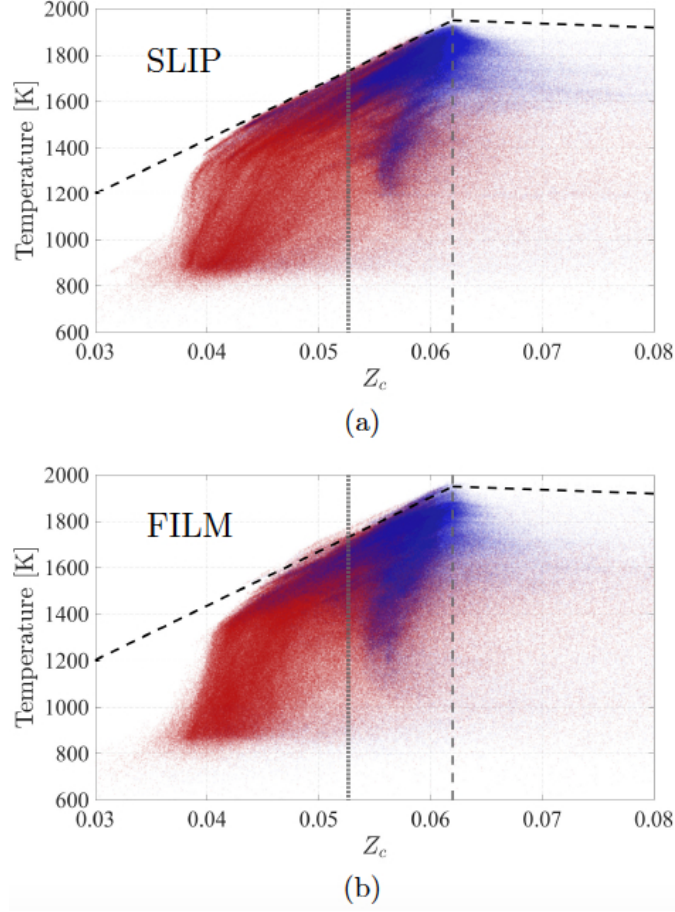


Figure 10: Scatter plot of the flame structure in the $T - Z$ plane for the SLIP (a) and FILM (b) cases. The color refers to different values of the Takeno index selecting the flame burning in premixed (red) or diffusive (blue) regimes. The two gray vertical line indicate the stoichiometric mixture fraction $Z^{st} = 0.062$ (dashed) and the one corresponding to the global equivalence ratio $Z^{85} = 0.0527$ (dotted), whereas the two adiabatic equilibrium lines are reported in black.

treatment, one observes that particles are mainly driven by the gaseous phase with the exception of the droplets with $d_p > 10 \mu\text{m}$ (reported in black diamonds) which detach from smaller particles due to inertia effects. It is also worth noting that these large droplets mainly locate on the outer tip part of the flame which will then favor the isolated droplet flames identified previously.

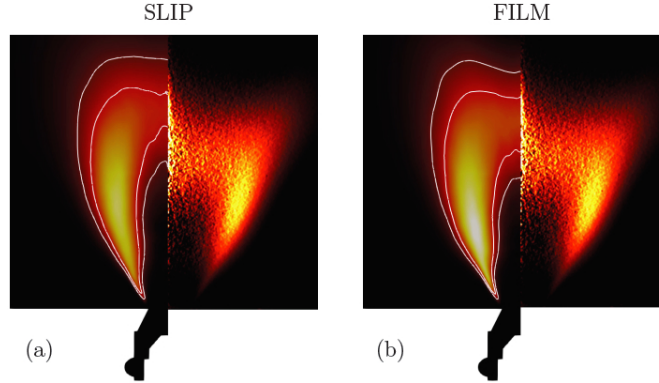


Figure 11: Comparison between LES angle and time-averaged flame shape, on the left, and CH^* chemiluminescence, on the right for SLIP (a) and FILM (b) cases.

To further compare droplet trajectory, the liquid volume fraction α_ℓ is displayed on a plane, containing the symmetry axis of the jet, in Fig. 13 for the SLIP (b) and FILM (c) cases respectively. One can see that particle trajectories can be of two different types, as sketched in Fig. 13 (a): most of the liquid phase injected hits the nearby injector wall (group \mathcal{P}_A) and only a small number of droplets follows the aerodynamic flowing directly in the combustion chamber (group \mathcal{P}_B). Note that the two different wall-interaction treatments will have an impact only on the droplets of the first group being the ones impinging the wall. Focusing the attention on this portion of liquid fuel, the effect of the different treatments can be observed comparing Fig. 13 (b) with (c). In the SLIP case, the liquid follows the angle of the injector wall after being detached at the edge and entering the combustion chamber, while for the FILM the detachment is regulated by the film model and the particles are released from the film treatment back into the gaseous phase with the film velocity component.

To conclude, the results presented in this section show that the treatment of the interaction between particles and walls does not have a major impact on the steady flame. The two simulations indeed show similar results and flame shapes as well as a similar dynamics of the liquid fuel in the combustion chamber, confirming that the aerodynamic field is the primary driver for the present particle distribution. The flame structure is also very similar in terms of combustion regimes and equivalence ratio spatial distribution, the field being mainly governed by the evaporation process. Differences mainly

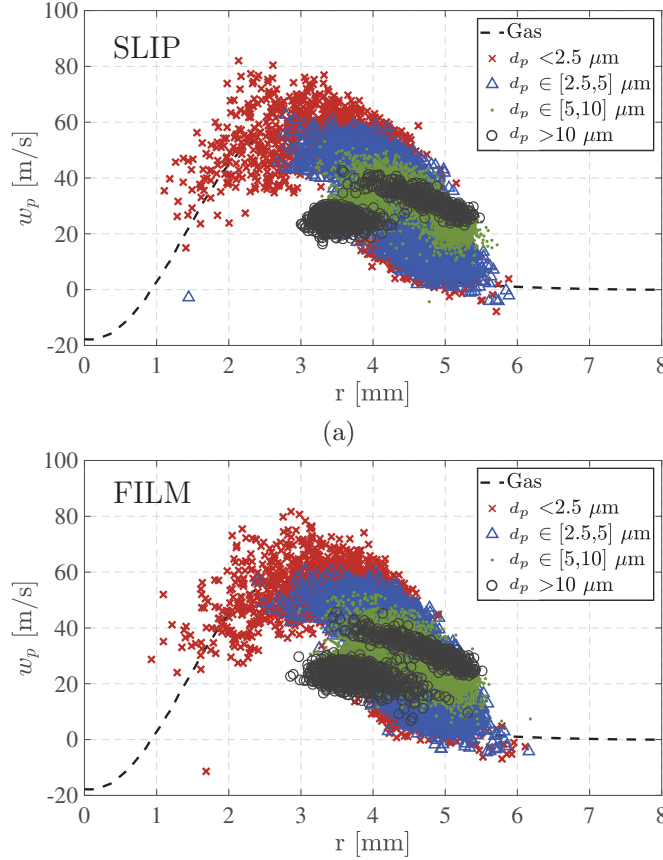


Figure 12: Liquid fuel properties at $z = 2.5$ mm from the backplane. Scatter of particles axial velocity compared with the gas mean profile (dashed line) for SLIP (a) and FILM (b) cases. In the SLIP case the post-processing is done on a time window of 11 ms resulting in $N_p = 11445$ while a longer time window of 13 ms is used for the FILM case to obtain a statistically similar number of droplets, i.e., $N_p = 13387$.

appear in the injection system. Depending on the particle-wall interaction model retained, the liquid fuel released at the edge of the injector seem to have different momentum. Therefore small changes in droplet trajectories can arise as shown by Fig. 13 but without impacting the flame regime or the anchoring process.

3.3. Thermoacoustic self-excited condition

The dynamic response of the two particle-wall treatment is now discussed in the context of thermo-acoustic combustion instabilities. In this case, the

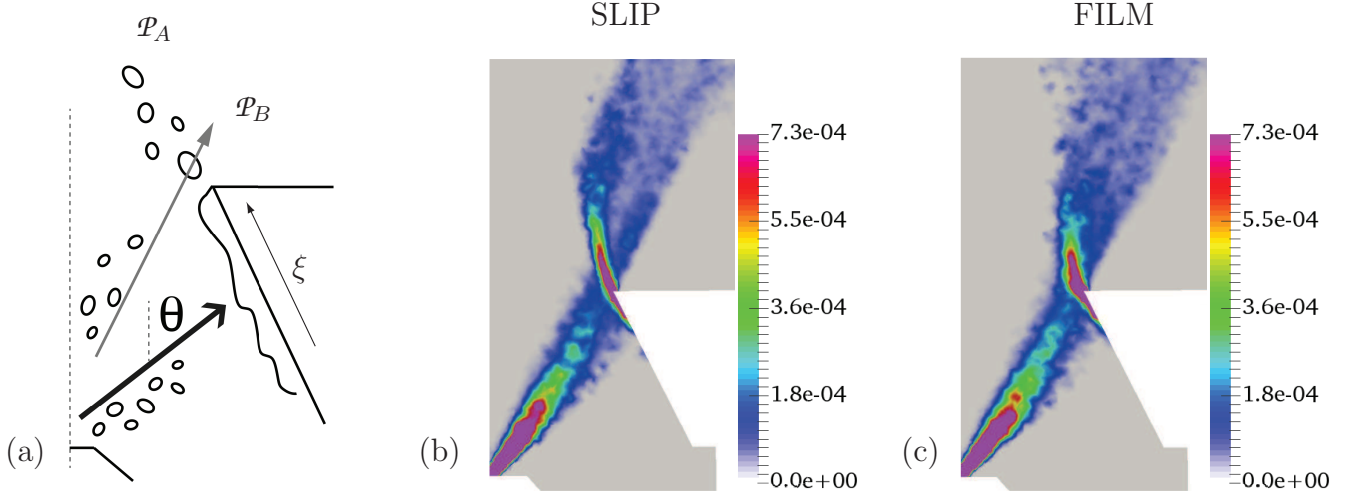


Figure 13: (a) Sketch of the two particles trajectories in a cut containing the symmetry axis. Liquid volume fraction $\rho_\ell \alpha_\ell$ for the SLIP (a) and FILM (b) cases.

two stable flames described in the Sect. 2 are considered but with a longer flame tube, a configuration in which a self-sustained limit cycle is observed in the experiment [28].

The limit cycle

Figure 14 (left) shows the temporal evolution of the pressure fluctuation evolution registered by a sensor located on the combustion chamber back-plane when the film treatment is used (case FILM). At the beginning of this specific simulation, the pressure signal features a classical exponential increase until a maximum pressure value (overshoot point) is reached [40]. The pressure oscillation then decreases until the energy generated by the thermo-acoustic coupling equals the system damping. Again for this specific case, after $t = 0.12$ s, the thermoacoustic oscillation can be considered established and a steady limit cycle condition is reached. A zoom on the simulation signal at latter time, Fig. 14 (right), shows indeed that the fluctuation of pressure and heat release are approximately in phase, satisfying the Rayleigh criterion [54] as expected in a thermo-acoustically unstable condition. It should be also noted that in the combustion chamber the level of the limit cycle, $p'_{LES} \simeq 2000$ Pa, is in line with the experimental measurements where a fluctuation amplitude of $p'_{exp} \simeq 1700$ Pa is recorded [27, 28].

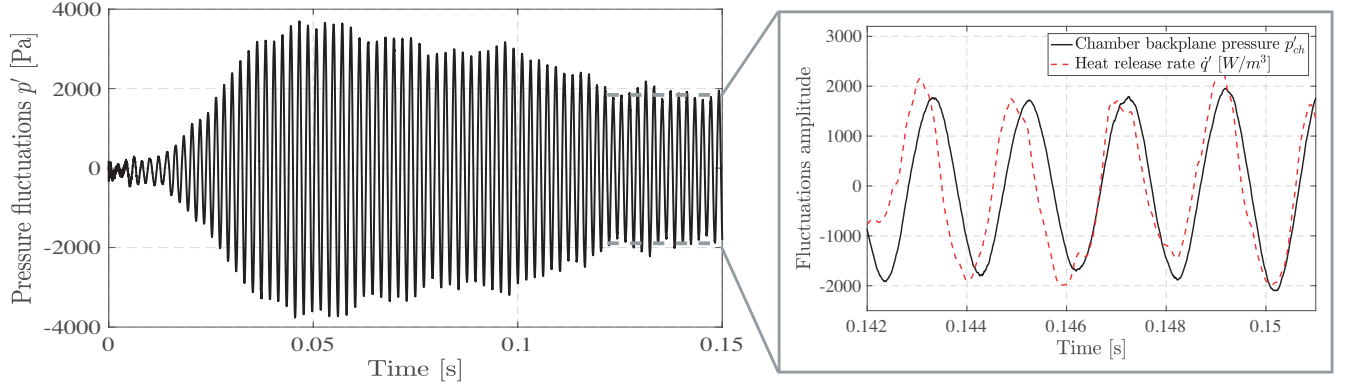


Figure 14: Pressure fluctuation measured at the combustion chamber backplane with a zoom on some cycles showing how the unsteady pressure and heat release rate oscillations present the same phase satisfying the Rayleigh criterion.



Figure 15: Acoustic mode obtained with Helmholtz solver.

Finally, the self-sustained operating condition yields a numerical oscillation at $f_{LES} \simeq 500$ Hz in decent agreement with the reported experimental value of $f_{EXP} = 530$ Hz [27, 28].

A preliminary simulation with the Helmholtz solver AVSP [55] was performed in passive flame conditions assuming cold conditions for the plenum and an average temperature of 1500 K in the combustion chamber (based on the LES simulations of the steady flame). To account for the scattering effect at the outlet, following previous works dealing with the same problem (e.g., see Ref [56] where an experimentally measured end-correction was applied to an annular combustion chamber to correctly retrieve the resonant mode frequencies), the combustion chamber length has been augmented by

Figure 16: Heat release rate phase average, colormap: $\dot{q} \in [0, 250]$ MW/m³, comparison with the experimental CH* chemiluminescence [27].

$l_{cc,corr} = 0.6 r_{cc} = 21$ [mm], which is the typical end-correction value for an unflanged circular pipe [57]. A pressure node condition ($p'=0$) is then imposed at the new outlet boundary. For sake of simplicity, a fully reflective inlet with $R=1$ is imposed at the inlet. A resonant mode with a frequency of $f \simeq 530$ Hz is retrieved from the eigenvalue analysis, value close to the one at which the numerical (and experimental) limit cycle occurs ($f_{LES} \simeq 500$ Hz). This result indicates that the observed dynamics are not associated to an intrinsic instability of the flame but they have an acoustic origin [58, 59]. It is noted that a high degree of decoupling between the two cavities is observed independently of the full reflectivity imposed at the inlet. The amplitude of the oscillation inside the combustion chamber therefore mainly depends on the swirler and chamber outlet acoustic properties. In LES, in order to focus the attention exclusively on the source of the thermoacoustic oscillation, the decoupling between the two-chambers is enforced by assuming a very low cutoff frequency: i.e. $f_c \simeq 0$ Hz which can be achieved by reducing the relaxation coefficient at the inlet boundary condition as discussed in the previous section. The fair agreement achieved with experimental results in terms of frequency, nature and combustion chamber pressure fluctuation level confirm the validity of these modelling assumptions.

In terms of flame shape, to remove random oscillations due to turbulence and retrieve only the coherent limit cycle oscillation, LES results are first phase-averaged over 10 cycles (Fig. 16). For each phase of the cycle, an angle average procedure is then performed. Note that in the following, the phase $\Phi \in [0, 2\pi]$ refers to the pressure signal oscillation for which $\Phi = \pi/2$ corresponds to the positive peak of heat release. Simulation results are finally compared to the experimental views from EM2C laboratory [27] in Fig. 16 proving the good agreement during the whole cycle for the overall flame shape, its extent as well as its anchoring position.

To conclude, even if a detailed comparison with the experimental data is out of the scope for this work, the LES and the experiment are found in fair agreement in terms of frequency, nature and combustion chamber pressure fluctuations confirming the validity of the modelling assumptions.

Modeling effect on the prediction

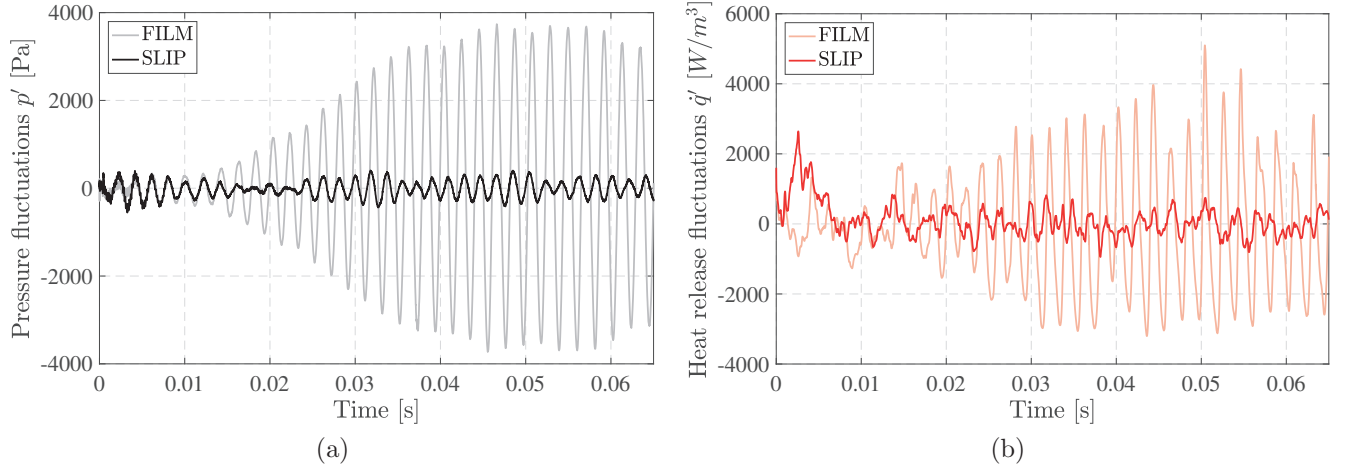


Figure 17: Comparison between the FILM and SLIP cases in resonating conditions. (a) Pressure fluctuation of the combustion chamber backplane as obtained for the two modelling approaches as well as (b) the temporal evolution of the heat release rate fluctuations. Both quantities are given as a function of time starting from the same initial flame and only the liquid-wall interaction treatment differs.

In agreement with the observations obtained for steady operating condition, the same calculation as the one discussed above is repeated changing only the particle-wall treatment: *i.e.* using the slip treatment in place of the film model (case SLIP). For the discussion, both transients are compared in Fig. 17, with (a) the time trace of the chamber pressure fluctuation for the backplane probe, (b) the fluctuating heat release rate per unit volume. In case of the SLIP condition traces of coherent oscillations are visible in the recorded pressure fluctuation as shown in Fig. 17 (a)(black line) for latter times. However, the mode growth observed in the previous simulation is not recovered and the oscillation amplitude remains very small and intermittent if compared to the one obtained using the film treatment (gray line in Fig. 17 (a)). More interestingly, coherence in the fluctuating heat release rate signal disappears very early in the SLIP case, as shown in Fig. 17 (b)(red line), while the film modelling provides sufficient response at longer times.

The absence of predominant oscillation frequency with the slip condition film treatment is verified by Fig. 18 (a) which shows the spectra of the heat release rate obtained for both simulations. The FFT confirms that the slip condition does not lead to a full synchronization of the heat release rate with the nearby acoustic mode. Indeed, multiple frequencies coexist including

lower and higher than the 500 Hz contribution which, instead, remains weak compared to the other simulation. Indeed, in the case of SLIP, the system and the harmonic oscillation last only for a short period of time. Figure 18 (b) which shows the superposition of the pressure time trace along with the fluctuating heat release as a function of the same time interval, confirms that the Rayleigh criterion is never fully satisfied but instead can be occasionally negative contrarily to the first simulation, as seen from Fig. 14. Using the film model instead, the system produces a coherent oscillation at $f_{LES} \simeq 500$ Hz (to be compared with the experimental value of $f_{EXP} = 530$ Hz [27]).

To eliminate any uncertainty regarding the initial condition another test was performed targeting the use of the slip treatment for droplets impinging the wall. Starting from the self-sustained unstable condition obtained with the film treatment, at time $t_{sw} \simeq 0.07$ s this film particle-wall interaction treatment is switched to slip. Looking at the corresponding temporal evolution presented in Fig. 19, the pressure fluctuation in the chamber backplane clearly gets damped after ten cycles and the system eventually reaches the same quasi-steady state as the one obtained previously. This second test is in the following used to better understand the effect of the film modelling by looking at the evolution of the liquid fuel distribution and properties inside the injection system at two specific instants and for the two cases of FILM ad SLIP. To do so, the liquid volume fraction α_ℓ is plotted for the two instants: *i.e.* $t_1 = t_{sw} + 3\mathcal{T}$ and $t_2 = t_{sw} + 10\mathcal{T}$, with \mathcal{T} the period of the thermoac-

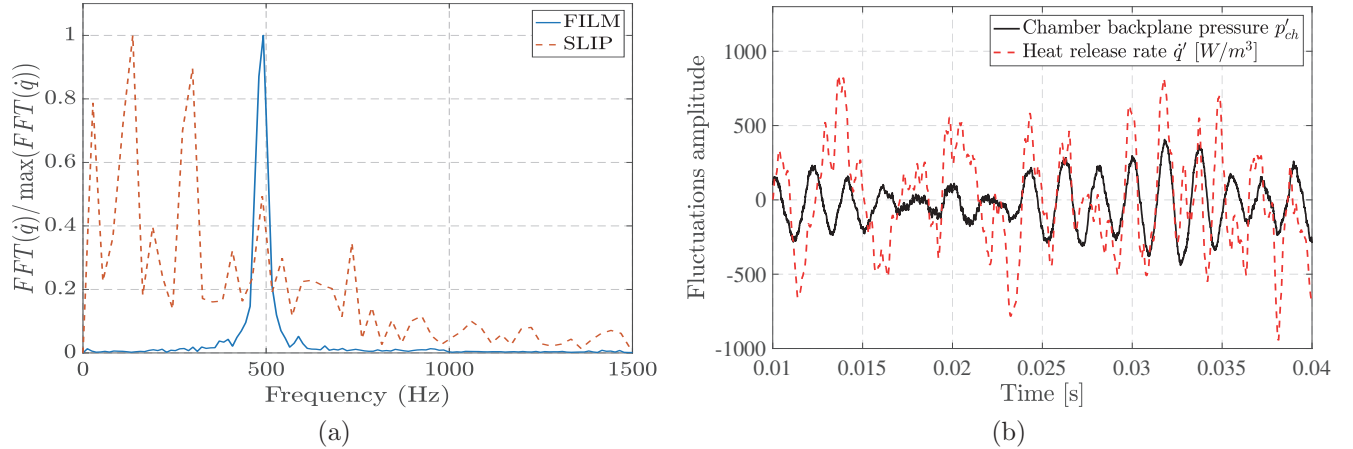


Figure 18: (a) FFT of the unsteady heat release rate using the two different cases and (b) unsteady heat release and pressure fluctuation for the SLIP case.

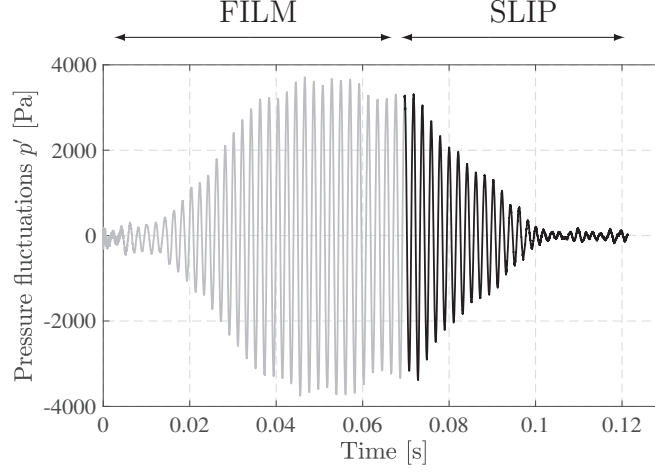


Figure 19: Pressure fluctuation signal at chamber backplane when the treatment is switched from film to slip.

coustic oscillation. Comparing the two different treatments, one notes that the amount of fuel trapped inside the system is kept almost constant after 10 cycles when the film modelling is adopted, Fig. 20 (a-b). On the contrary, when the condition is slip, particles are still in the injector 3 cycles after t_{sw} , Fig. 20 (c), but these trapped particles are rapidly washed away by the strong aerodynamics oscillations and after few other cycles, Fig. 20 (d). The injector wall is almost clean of particles except near the edge at latter times. This brings to the conclusion that as long as droplets are trapped in the near injector region the oscillation remains high, but as soon as the slip condition prevails, the liquid trapped in this region starts entering the combustion chamber almost without delay precluding a clear establishment of the oscillation.

Focusing now on the distribution of liquid volume fraction α_ℓ at the edge of the injector shown in Fig. 20, droplet behaviours and therefore the thermoacoustic response of the system mainly appears to be controlled by the chosen wall treatment. Indeed, in case SLIP, Fig. 20 (c-d) shows that, at longer times, after impacting with the wall, particles penetrate the main stream jet entering the combustion chamber closer to the jet axis before being accelerated by the radial component of the jet. This is not the case when the film treatment is adopted, Fig. 20 (a-b).

Figure 21 shows the droplet velocity magnitude confirming once more

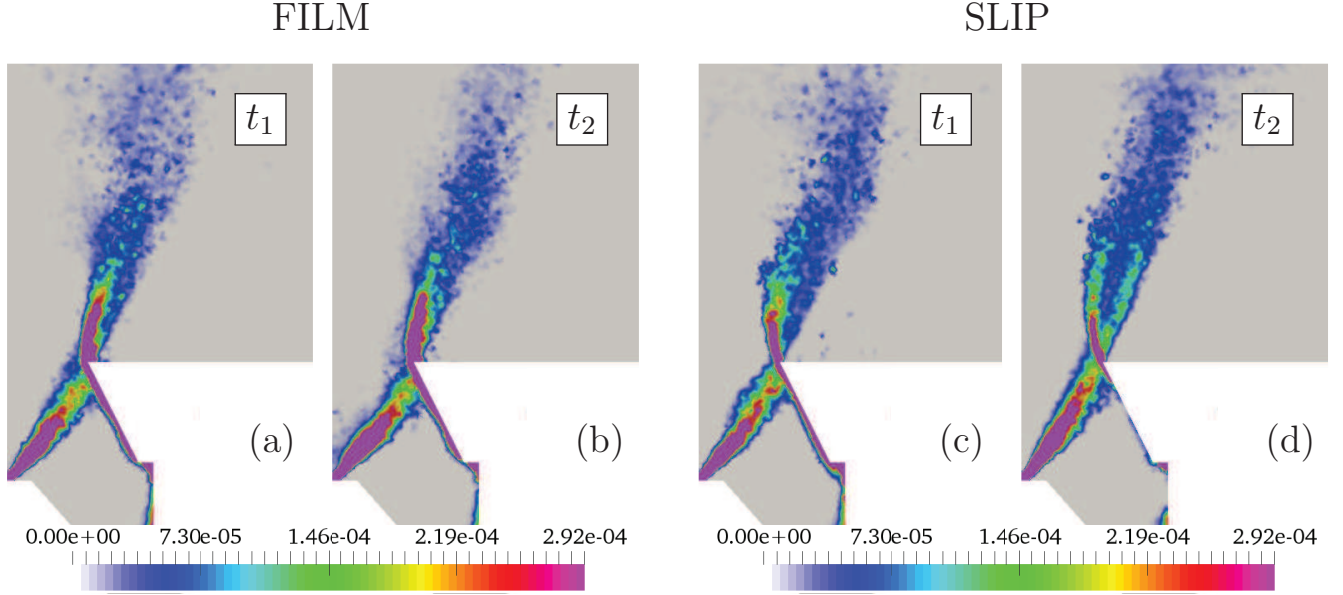


Figure 20: Liquid volume fraction, α_ℓ , at $t_1 = 0.078$ ms and $t_2 = 0.1$ ms for the simulations for FILM (a)-(b) and SLIP (c)-(d) cases.

that the application of a slip model does not slow down the liquid impinging the wall before entering the combustion chamber. Note from Fig. 21 (c) that some particles although being part of the remaining film layer, already at time t_1 , present high velocities in the combustion chamber $|\vec{v}_p| \geq 30$ m/s. At latter times even faster particles appear, Fig. 21 (d), and the presence of high speed droplets further downstream in the combustion chamber increases the stiffness to the external modulation of the liquid fuel entering the combustion chamber. Its propensity to couple with the thermoacoustic oscillation is therefore reduced.

As shown in the next section, the difference of relative velocity between the liquid and the gaseous phase near the walls helps triggering the thermoacoustic mode of this configuration. In that respect, only the film treatment is able to reproduce the proper effect, being the response of the film affected by the acoustic oscillation. The slip condition instead is not able to capture this complex dynamics letting the droplets enter the combustion chamber without being modulated by the presence of acoustics in the system.

Effect of the film on the thermoacoustic loop

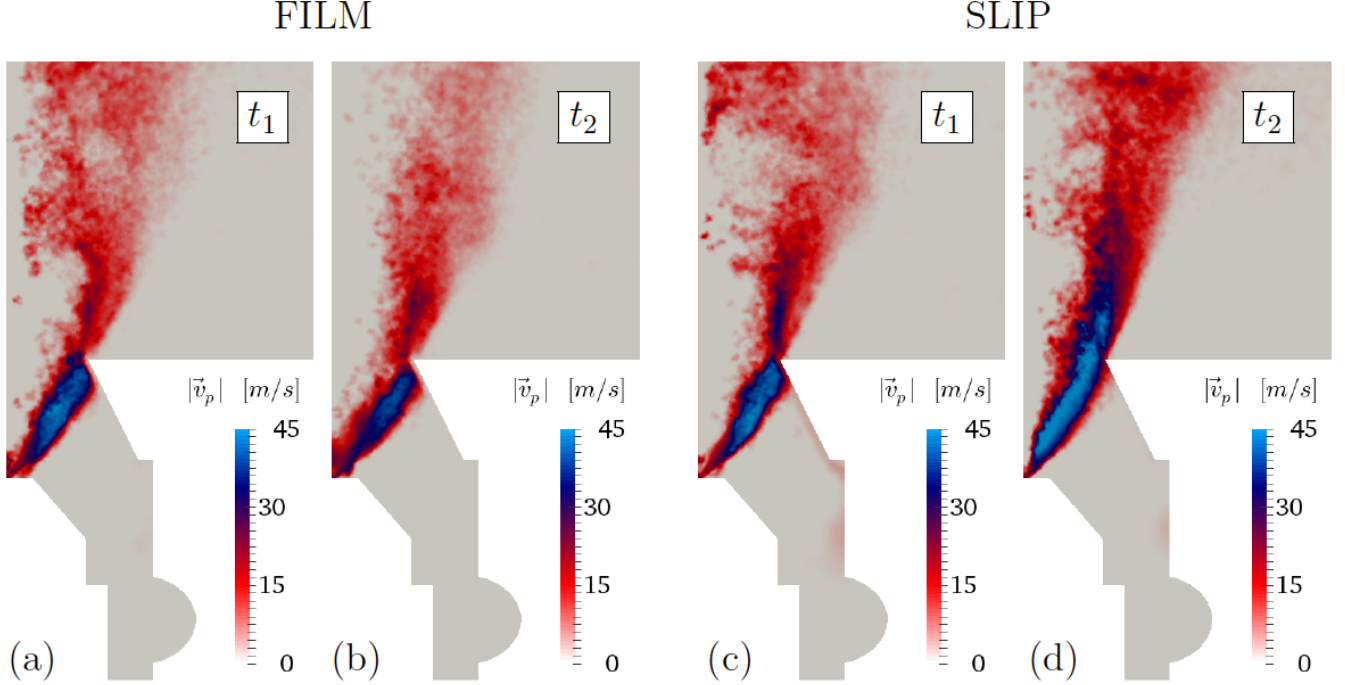


Figure 21: Liquid velocity magnitude, \vec{v}_p , at $t_1 = 0.078\text{ ms}$ and $t_2 = 0.1\text{ ms}$ respectively for the simulations for FILM (a)-(b) and SLIP (c)-(d) cases.

The previous analysis suggests the fundamental importance of the film response in the presence of an external acoustic field. Assuming that the local aerodynamics is the same for both simulations, the quantity characterizing the film response is its thickness, h_f . Figure 22 (a) displays the film thickness fluctuation h' as a function of the film coordinate ξ (*cf.* Fig. 13 (a)) and obtained at different instants in the limit-cycle period of the simulation. This quantity is clearly fluctuating within an envelop corresponding to the phase $\Phi = 0$ and 2π if referring to the definition introduced for Fig. 16. The other observation is that this film layer only responds to acoustics in its second half, that is for $\xi \in [4.5, 7]$, where large variations of h' are achieved. Based on such observations, some interesting quantities relative to this film oscillation as its characteristic frequency, noted f_f , can be proposed. First, taking the average film velocity along the axial film coordinate ξ , $U_f \simeq 1.3\text{ m/s}$, and considering the length of the oscillating film layer only, $l_f^{osc} = 2.5\text{ mm}$, the film characteristic frequency reads $f_f = U_f/l_f = 520\text{ Hz}$. This simple evalu-

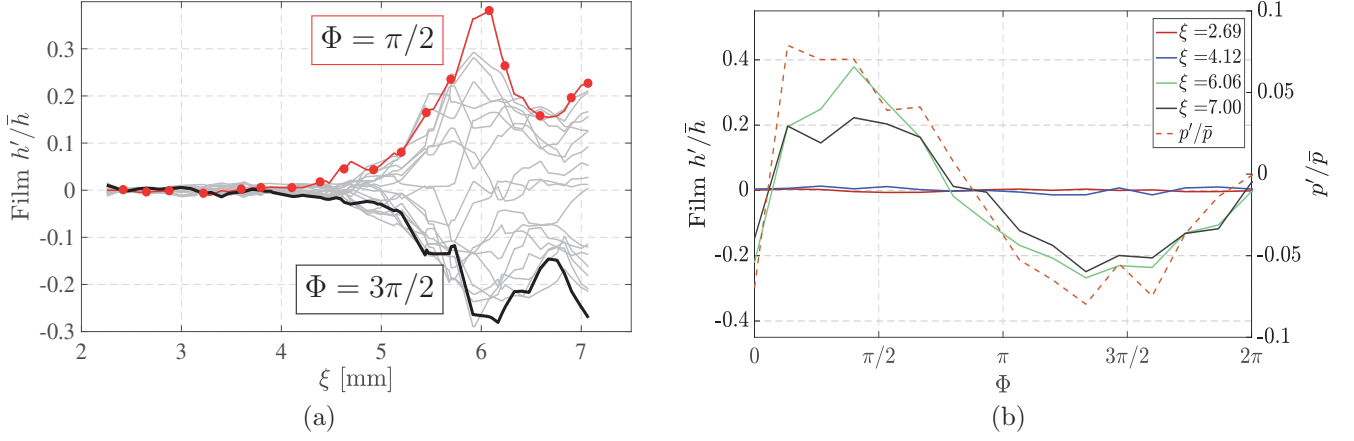


Figure 22: (a) Non-dimensional film height fluctuation, h'/\bar{h} , along the film local coordinate ξ during the period of oscillation. (b) Non-dimensional film height fluctuation, h'/\bar{h} , measured at different locations along the film, plot in phase with the mode pressure signal p'/\bar{p} properly rescaled.

ation of the film convective timescale confirms that during the limit cycle the film response synchronizes with the thermoacoustic loop suggesting that this dynamic may be a key parameter when willing to control the thermoacoustic oscillation. Future studies will focus on the effect of the variations of some liquid injection parameters showing the impact on the different film responses. The effects of such variations on the whole thermoacoustic mechanism is not trivial since the synchronization between the release of fuel and the heat release is controlled by the local aerodynamics and pressure oscillation which are finally connected to the thermoacoustic feedback loop. The response of the film is further confirmed by Fig. 22 (b) where the phase averaged film thickness fluctuation is shown as a function of the mode acoustic pressure phase during the cycle and for various axial locations within the film. Clearly only the second half of the film exhibits thickness variations that are in phase with the local pressure signal identified as p'/\bar{p} in Fig. 22 (b).

Figure 23(a) reports the fluctuation of the non-dimensional equivalence ratio at an axial station near the flame root ($z = 2.5$ mm). If compared with the previously discussed film thickness dynamics (Fig. 22(a)), it is possible to notice that the two variables oscillate in phase (to improve the visualisation of this result, the curves corresponding to $\phi = \pi/2$ and $\phi = 3/2\pi$ have the same color in both images). An explanation of this result is retrieved recalling the film modelling presented in Sec. 2.2. As indicated by Eq. (6), film thickness

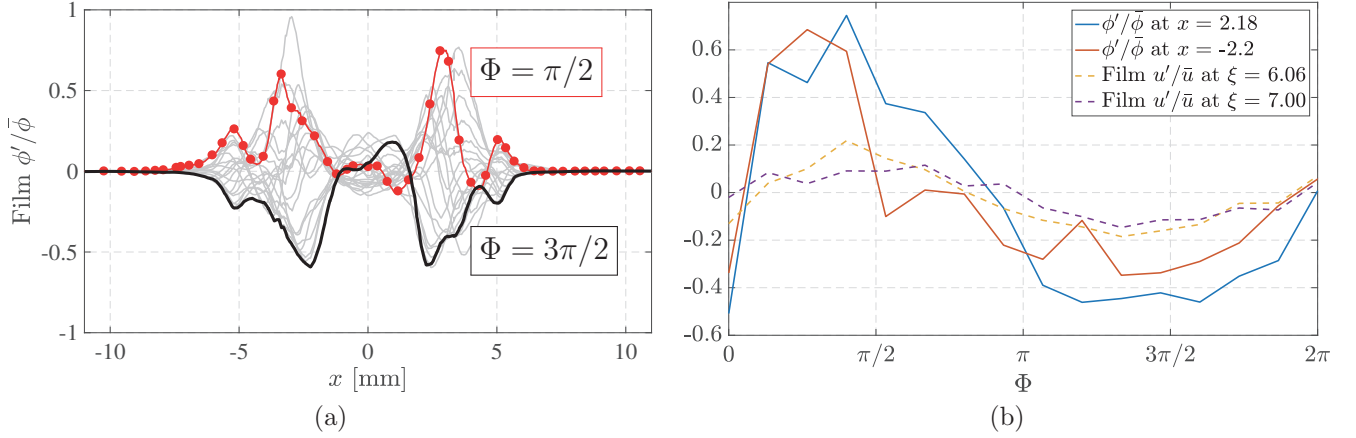


Figure 23: (a) Non-dimensional equivalence ratio fluctuations, $\phi'/\bar{\phi}$, as a function of the radial coordinate x , measured at the flame root ($z = 2.5$ mm) during the period of oscillation. (b) Non-dimensional equivalence ratio fluctuations, $\phi'/\bar{\phi}$, at the flame root plot in phase with film velocity fluctuations, u'/\bar{u} , at the edge of the film layer.

fluctuation and constant wall shear stress result in a film velocity fluctuation and therefore the release of particles at the edge of the injector with different velocities tuned by the limit cycle. Figure 23 (b) shows as a consequence of the film velocity fluctuation (dashed line: u'/\bar{u} near the injector lip) the fluctuation of equivalence ratio near the flame root (full lines: $\phi'/\bar{\phi}$ taken at two radial coordinates). As intuited above both quantities are in phase revealing the major impact on the fuel feeding of the flame root dynamics.

In other words the feedback to the thermoacoustic mode involves the film response which needs to be taken into account through modelling. Indeed, the film thickness and therefore the particle velocity composing the film introduce a dependency of the fuel feeding process of the combustion chamber, the heat release and potentially the system pressure fluctuation field.

In Fig. 24, fields of heat release (a) are provided along with fields of total equivalence ratio (b) at various phases of the obtained numerical prediction. In agreement with the scenario detailed previously, higher levels of heat release fluctuations coincide with the release by the film of a large number of particles in the chamber ($\Phi \in [0 - \pi]$). On the contrary at later times ($\Phi = [\pi, 2\pi]$), the swirler flow aerodynamics pushes the flow back in the combustion chamber almost cancelling the negative velocity region (CRZ). For this part of the cycle, the flame shortens consuming the previously evaporated gaseous fuel present in the chamber ($\Phi = 3\pi/2$) since, at this point of the cycle, the fuel is trapped in the injection system and in particular in

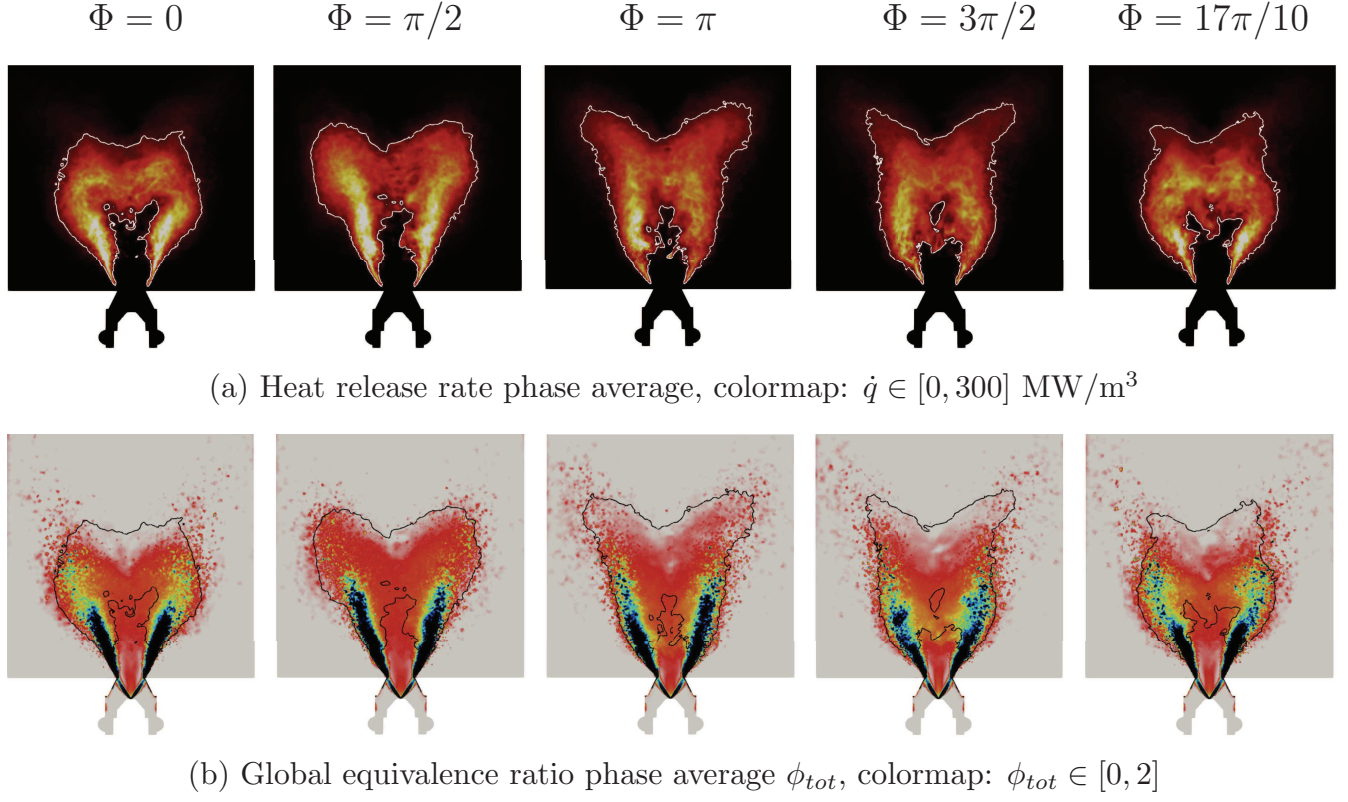


Figure 24: Phase averaged (a) heat release distribution and (b) overall equivalent ration during the limit cycle; added contours indicate the $\dot{q} = 50$ MW/m³ release rate location.

the film layer, until $\Phi = 17\pi/10$ where the heat release rate increases again entering a new cycle.

A final observation of interest focuses on the overall fluid mechanics response of the system and its effect on the particle distribution within the combustion chamber during the cycle. As indicated previously, the film is a key element in determining the proper response of SICCA-spray but so does the aerodynamics and more particularly the fuel distribution, both evaporated and liquid, in the combustor. To evidence and emphasize this last aspect Fig. 25 displays the temporal evolution of the fluctuating number of particles around the mean and presents their evolution for different axial planes away from the chamber backplane. For the lower planes, *i.e.* in the injector exit region or $z = 2.5$ & 4 mm away from the chamber backplane, more droplets are released in the early instants of the mode in agreement with

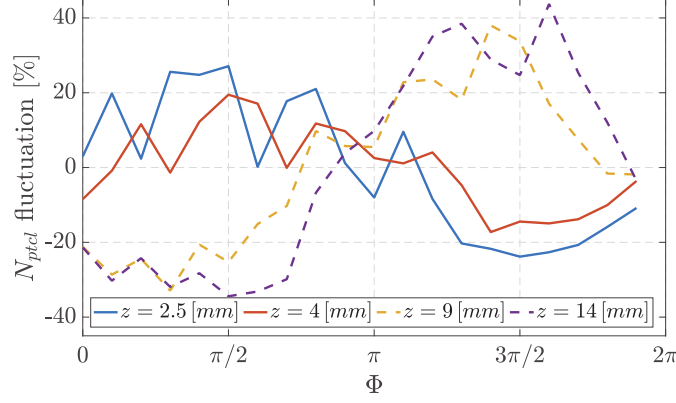


Figure 25: Fluctuations of the droplets number during the limit cycle at different location from the backplane.

previous findings: *i.e.* in phase with the reference pressure signal. Further away in the chamber, *i.e.* $z = 9$ & 14 mm, the response is out of phase with the pressure signal indicating that either the number of droplets initially injected are consumed, and/or evaporated, or it takes them time to reach this position.

4. Conclusions

The lean two-phase swirled flames of the SICCA-spray experiment is simulated by use of a Lagrangian LES formalism for both steady and self-sustained limit-cycle operating conditions. It has been proven, for this specific experimental setup, the capability of the Lagrangian approach to fully represent these problems and the independency of the results to the wall treatment when simulating the steady conditions. When willing to simulate the thermoacoustic oscillation the slip wall treatment is proven to be incapable of reproducing the dynamic response of the liquid fuel impinging on the wall, whereas adopting a film model allows to overcome this limit. Consequently, in the resonating condition the slip treatment fails to reproduce the thermoacoustic instability, leading to limit cycle, observed experimentally not only when the instability is willing to occur but also when the unstable regime is already established. In this second test, the case SLIP results in a system that gets damped after few cycles with fluctuation levels that are far from the experimental observations and not self-sustained. On the contrary, the limit cycle is accurately reproduced in the case FILM. Indeed,

it is proven that with the film treatment the liquid sheet velocity is significantly reduced, if compared to the other case, and the delay imposed to the liquid impinging the wall before entering the combustion chamber synchronizes with the thermoacoustic oscillation. Moreover, the capability of the film treatment to adapt the liquid sheet properties to the self-sustained oscillation indicates that the fuel film layer is responding to the external flow fluctuations ensuring a closed feedback loop with the thermoacoustics of the entire system and therefore the establishment of the self-sustained limit-cycle.

Acknowledgements and Fundings

This project has received funding from the European Union Horizon 2020 research and innovation program under the Marie Skłodowska-Curie grant agreement No 765998 in the project ANNULIGH T. The authors gratefully acknowledge the financial support from Agence Nationale de la Recherche (ANR) under the project FASMIC (ANR16-CE22-0013). D. Laera is grateful to the European Union Horizon 2020 for financial support under the Marie Skłodowska-Curie Individual Fellowship grant agreement No 843958 in the project CLEANERFLAMES. This work was performed using HPC resources from GENCI (Grant 2020-A0052B10157). Particular gratitude goes to T. Laroche and J. Carmona who participated with useful discussions and active effort in optimizing the film boundary condition and to the whole CERFACS team developing AVBP. The authors also thank Daniel Durox and the team performing experiments at EM2C in Paris for the availability and the share of data and ideas.

Appendix A: The code AVBP with Euler-Lagrange formalism

The LES code AVBP solves the full compressible Navier-Stokes equations with spatial filtering:

$$\frac{D}{Dt}(\bar{\rho}\tilde{\mathbf{u}}) = -\nabla \cdot (\bar{p}\mathbf{I} - \bar{\mathbf{T}} - \bar{\mathbf{T}}^{sgs}) + \bar{\mathbf{s}}_M \quad (7)$$

$$\frac{D}{Dt}(\bar{\rho}E) = -\nabla \cdot (\overline{\mathbf{u} \cdot \bar{p}\mathbf{I} - \bar{\mathbf{T}} + \bar{\mathbf{q}} + \bar{\mathbf{q}}^{sgs}}) + \bar{s}_E \quad (8)$$

$$\frac{D}{Dt}(\bar{\rho}\tilde{Y}_k) = -\nabla \cdot (\bar{\mathbf{j}}_k + \bar{\mathbf{j}}_k^{sgs}) + \bar{s}_{Y_k} \quad k = 1, N_S \quad (9)$$

where the Favre filtering $\tilde{f} = \overline{\rho f} / \bar{\rho}$ weights with density the Reynolds filtered variables \tilde{f} . $\frac{D}{Dt} = \frac{\partial}{\partial t} + \tilde{\mathbf{u}} \cdot \nabla$ is the total derivative, \mathbf{I} is the identity matrix and the terms $\bar{\mathbf{s}}_M$, $\bar{\mathbf{s}}_E$ and $\bar{\mathbf{s}}_{Y_k}$ are the exchange terms between gaseous and liquid phase. $\bar{\mathbf{T}}$ is the filtered stress tensor, $\bar{\mathbf{j}}_k$ is the species flux according to [40] while $\bar{\mathbf{q}}$ accounts of heat fluxes due to differential diffusion of species and temperature. Subgrid scale closure is modelled as:

$$\bar{\mathbf{T}}^{sgs} = \bar{\rho}(\widetilde{\mathbf{u} : \mathbf{u}} - \tilde{\mathbf{u}} : \tilde{\mathbf{u}}) \simeq 2\bar{\rho}\nu_t \left(\tilde{\mathbf{S}} - \frac{1}{3}tr(\tilde{\mathbf{S}})\mathbf{I} \right) \quad (10)$$

$$\bar{\mathbf{j}}_k^{sgs} = \bar{\rho}(\widetilde{Y_k \mathbf{u}} - \tilde{Y}_k \tilde{\mathbf{u}}) \simeq 2\bar{\rho} \left(D_t \frac{W_k}{W} \nabla \tilde{X}_k - \tilde{Y}_k \mathbf{V}^c \right) \quad (11)$$

$$\bar{\mathbf{q}}^{sgs} = \bar{\rho}(\widetilde{E \mathbf{u}} - \tilde{E} \tilde{\mathbf{u}}) \simeq -\lambda_t \nabla \tilde{T} + \sum_{k=1}^{N_S} \bar{\mathbf{j}}_k^{sgs} \tilde{h}_{s,k} \quad (12)$$

where the turbulent eddy viscosity ν_t is computed according to [34] and the coefficients for species and temperature are computed imposing the turbulent Prandtl and Shmidt numbers to 0.6 from $D_t = \nu_t / Sc^t$ and $\lambda_t = \bar{\rho} \nu_t \overline{C_p} / Pr^t$. The Lagrangian formalism for the liquid phase reads

$$\frac{d\mathbf{x}_p}{dt} = \mathbf{u}_p \quad , \quad \frac{d\mathbf{u}_p}{dt} = \frac{\mathbf{f}_p}{m_p} \quad (13)$$

where \mathbf{x}_p is the particle position, \mathbf{u}_p its velocity, m_p its mass and \mathbf{f}_p the sum of forces acting on each particles which here is considered to be drag only. Evaporation is handles by a mass balance such as

$$\frac{dm_p}{dt} = \dot{m}_p \quad , \quad \frac{dT_p}{dt} = -\frac{1}{m_p C_{p,l}} \phi_p^c \quad (14)$$

where \dot{m}_p is the evaporation rate, $C_{p,l}$ the liquid specific heat and ϕ_p^c the conductive heat flux to be exchanged with the gaseous phase.

The exchange terms assume the form [60]

$$\bar{\mathbf{s}}_M = -\frac{1}{V} \sum_{p=1}^{N_p} w_{p@n} (\dot{m}_p \mathbf{u}_p + \mathbf{f}_p) \quad (15)$$

$$\bar{\mathbf{s}}_E = -\frac{1}{V} \sum_{p=1}^{N_p} w_{p@n} \left(\phi_p^c - \dot{m}_p h_{s,F}(T_p) + \frac{1}{2} \dot{m}_p \mathbf{u}_p^2 + \mathbf{f}_p \cdot \mathbf{u}_p \right) \quad (16)$$

$$\bar{\mathbf{s}}_{Y_k} = -\frac{1}{V} \sum_{p=1}^{N_p} w_{p@n} (\dot{m}_p \delta_{k,F}) \quad (17)$$

where $w_{p@n}$ is the conservative weight for the particle p with respect the node n , ϕ^c is the heat flux from at the droplet surface such that $\phi_p^c = -\phi^c + \dot{m}_p L_v(T_p)$ with L_v the droplet latent heat of vaporization. Closure for the evaporation term \dot{m}_p and for the flux term ϕ^c is given by

$$\dot{m}_p = -\pi d \text{Sh} [\rho D_F] \ln(1 + B_M) \quad (18)$$

$$\phi^c = -\pi d \text{Nu} \lambda (T_\infty - T_p) \frac{\ln(1 + B_T)}{B_T} \quad (19)$$

as in [61], [62] with B_M and B_T the Spalding numbers of mass and temperature according to [63]. It is noted that the impact of sub-grid fluctuations on velocity, temperature, droplet drag and evaporation rate is assumed negligible.

References

- [1] T. Lieuwen, V. Yang (Eds.), Combustion instabilities in gas turbine engines: operational experience, fundamental mechanisms and modeling, Progress in astronautics and aeronautics, American Institute of Aeronautics and Astronautics, Reston, VA, USA, 2005.
- [2] S. Candel, Combustion dynamics and control: Progress and challenges, Proc. Combust. Inst. 29 (1) (2002) 1–28.
- [3] A. P. Dowling, S. R. Stow, Acoustic analysis of gas turbine combustors, J. Propul. Power 19 (5) (2003) 751–764.
- [4] M. Bauerheim, F. Nicoud, T. Poinsot, Progress in Anal. Methods to predict and control azimuthal combustion instability modes in annular chambers, Phys. Fluids 28 (2) (2016) 021303.
- [5] J. Li, A. S. Morgans, Time domain simulations of nonlinear thermoacoustic behaviour in a simple combustor using a wave-based approach, J. Sound Vib. 346 (1) (2015) 345–360.
- [6] G. Staffelbach, L. Gicquel, G. Boudier, T. Poinsot, Large eddy simulation of self excited azimuthal modes in annular combustors, Proc. Combust. Inst. 32 (2) (2009) 2909–2916.

- [7] P. Wolf, G. Staffelbach, L. Y. Gicquel, J.-D. Müller, T. Poinso, Acoustic and Large Eddy Simulation studies of azimuthal modes in annular combustion chambers, *Combust. Flame* 159 (11) (2012) 3398–3413.
- [8] D. Noh, E. Karlis, S. Navarro-Martinez, Y. Hardalupas, A. Taylor, D. Fredrich, W. Jones, Azimuthally-driven subharmonic thermoacoustic instabilities in a swirl-stabilised combustor, *Proc. Combust. Inst.* 37 (4) (2019) 5333–5341.
- [9] D. Fredrich, W. P. Jones, A. J. Marquis, The stochastic fields method applied to a partially premixed swirl flame with wall heat transfer, *Combust. Flame* 205 (2019) 446–456.
- [10] T. Poinso, Prediction and control of combustion instabilities in real engines, *Proc. Combust. Inst.* 36 (1) (2017) 1–28.
- [11] T. Lieuwen, *Unsteady Combustor Physics*, Cambridge Univ Press, 2012.
- [12] W. Jones, A. Marquis, D. Noh, A stochastic breakup model for large eddy simulation of a turbulent two-phase reactive flow, *Proc. Combust. Inst.* 36 (2) (2017) 2559–2566.
- [13] A. Giusti, E. Mastorakos, Detailed chemistry LES/CMC simulation of a swirling ethanol spray flame approaching blow-off, *Proc. Combust. Inst.* 36 (2) (2017) 2625–2632.
- [14] G. Eckel, J. Grohmann, L. Cantu, N. Slavinskaya, T. Kathrotia, M. Rachner, P. Le Clercq, W. Meier, M. Aigner, LES of a swirl-stabilized kerosene spray flame with a multi-component vaporization model and detailed chemistry, *Combust. Flame* 207 (2019) 134–152.
- [15] A. Innocenti, A. Andreini, B. Facchini, A. Peschiulli, Numerical analysis of the dynamic flame response of a spray flame for aero-engine applications, *Int. J. Spray Combust. Dyn.* 9 (4) (2017) 17568277–1770357.
- [16] M. Boileau, S. Pascaud, E. Riber, B. Cuenot, L. Y. M. Gicquel, T. J. Poinso, M. Cazalens, Investigation of two-fluid methods for large eddy simulation of spray combustion in gas turbines, *Flow, Turbul. Combust.* 80 (3) (2008) 291–321.

- [17] A. Kaufmann, M. Moreau, O. Simonin, J. Hélie, Comparison between lagrangian and mesoscopic eulerian modelling approaches for inertial particles suspended in decaying isotropic turbulence, *J. Comput. Physics* 227 (2008) 6448–6472.
- [18] A. Ghani, T. Poinso, L. Gicquel, G. Staffelbach, LES of longitudinal and transverse self-excited combustion instabilities in a bluff-body stabilized turbulent premixed flame, *Combust. Flame* 162 (11) (2015) 4075–4083.
- [19] F. Ham, S. V. Apte, G. Iaccarino, X. Wu, M. Herrmann, G. Constantinescu, K. Mahesh, P. Moin, Unstructured LES of reacting multiphase flows in realistic gas turbine combustors, in: *Annual Research Briefs, Center for Turbulence Research, Center for Turbulence Research, NASA Ames/Stanford Univ.*, 2003, pp. 139–160.
- [20] F. Collin-Bastiani, J. Marrero-santiago, E. Riber, G. Cabot, A joint experimental and numerical study of ignition in a spray burner, *Proc. Combust. Inst.* 37 (4) (2018) 5047–5055.
- [21] S. Tachibana, K. Saito, T. Yamamoto, M. Makida, T. Kitano, Experimental and numerical investigation of thermo-acoustic instability in a liquid-fuel aero-engine combustor at elevated pressure : Validity of large-eddy simulation of spray combustion, *Combust. Flame* 162 (6) (2015) 2621–2637.
- [22] J. M. Apeloig, F.-X. D’Herbigny, F. Simon, P. Gajan, M. Orain, S. Roux, Liquid-Fuel Behavior in an Aeronautical Injector Submitted to Thermoacoustic Instabilities, *J. Propuls. Power* 31 (1) (2014) 309–319.
- [23] C. Clanet, G. Searby, P. Clavin, Primary acoustic instability of flames propagating in tubes: cases of spray and premixed gas combustion, *J. Fluid Mech.* 385 (1999) 157–197.
- [24] T. Kitano, K. Kaneko, R. Kurose, S. Komori, Large-eddy simulations of gas- and liquid-fueled combustion instabilities in back-step flows, *Combust. Flame* 170 (2016) 63–78.
- [25] A. H. Lefebvre, *Atomization and Spray*, CRC Press, 1989.

- [26] P. D. Hede, P. Bach, A. D. Jensen, Two-fluid spray atomisation and pneumatic nozzles for fluid bed coating/agglomeration purposes: A review, *Chem. Eng. Sci.* 63 (14) (2008) 3821–3842.
- [27] K. Prieur, *Dynamique de la combustion dans un foyer annulaire multi-injecteurs diphasique*, 2017, Université Paris-Saclay.
- [28] K. Prieur, D. Durox, G. Vignat, T. Schuller, S. Candel, Experimental determinations of flame describing functions of swirling spray flames., in: *Colloque INCA*, 2017, Châteaufort, France, 2017. doi:hal-02324581.
- [29] G. Vignat, D. Durox, K. Prieur, S. Candel, An experimental study into the effect of injector pressure loss on self-sustained combustion instabilities in a swirled spray burner, *Proc. Combust. Inst.* 37 (4) (2018) 5205–5213.
- [30] K. Prieur, D. Durox, T. Schuller, S. Candel, Strong azimuthal combustion instabilities in a spray annular chamber with intermittent partial blow-off, *J. Eng. Gas Turbines Power* 140 (3) (2017) 031503.
- [31] O. Colin, M. Rudgyard, Development of high-order taylor-galerkin schemes for les, *J. Comput. Phys.* 162 (2) (2000) 338–371.
- [32] T. J. Poinso, S. Lele, Boundary conditions for direct simulations of compressible viscous flows, *J. Comput. Phys.* 101 (1) (1992) 104–129.
- [33] L. Selle, F. Nicoud, T. Poinso, Actual Impedance of Nonreflecting Boundary Conditions: Implications for Computation of Resonators, *AIAA J.* 42 (5) (2004) 958–964.
- [34] F. Nicoud, F. Ducros, Subgrid-scale stress modelling based on the square of the velocity gradient tensor, *Flow, Turbul. Combust.* 62 (3) (1999) 183–200.
- [35] M. D. Paulhiac, B. Cuenot, E. Riber, L. Esclapez, S. Richard, Analysis of the spray flame structure in a lab-scale burner using Large Eddy Simulation and Discrete Particle Simulation., *Combust. Flame* 212 (2020) 25–38.

- [36] B. Rochette, F. Collin-Bastiani, L. Gicquel, O. Vermorel, D. Veynante, T. Poinso, Influence of chemical schemes, numerical method and dynamic turbulent combustion modeling on LES of premixed turbulent flames, *Combust. Flame* 191 (2018) 417–430.
- [37] F. Charlette, C. Meneveau, D. Veynante, A power-law flame wrinkling model for LES of premixed turbulent combustion Part II: dynamic formulation, *Combust. Flame* 131 (1-2) (2002) 181–197.
- [38] B. Rochette, E. Riber, B. Cuenot, Effect of non-zero relative velocity on the flame speed of two-phase laminar flames, *Proc. Combust. Inst.* 37 (3) (2019) 3393–3400.
- [39] H. Yamashita, M. Shimada, T. Takeno, A numerical study on flame stability at the transition point of jet diffusion flames, *Symp. Int. Combust. Proc.* 26 (1) (1996) 27–34.
- [40] T. Poinso, D. Veynante, *Theoretical and numerical combustion*, RT Edwards, Inc., 2005.
- [41] M. D. Paulhiac, *Modelisation de la Combustion d’un Spray dans un Bruleur Aéronautique*, INPT, 2015.
- [42] L. Schiller, A. Naumann, A drag coefficient correlation, *Zeitschrift des Vereins Deutscher Ingenieure* 77 (1935) 318–320.
- [43] B. Abramzon, W. Sirignano, Droplet vaporization model for spray combustion calculations, *Int. J. Heat Mass Tran.* 32 (9) (1989) 1605–1618.
- [44] G. Hannebique, P. Sierra, E. Riber, B. Cuenot, Large Eddy Simulation of Reactive Two-Phase Flow in an Aeronautical Multipoint Burner, *Flow, Turbul. Combust.* 90 (2) (2013) 449–469.
- [45] A. Moreira, A. Moita, M. Panao, Advances and challenges in explaining fuel spray impingement: How much of single droplet impact research is useful?, *Prog. Energy Combust. Sci.* 36 (5) (2010) 554–580.
- [46] D. Kalantari, C. Tropea, Spray impact onto flat and rigid walls: Empirical characterization and modelling, *Int. J. Multiph. Flow* 33 (5) (2007) 525–544.

- [47] L. Gao, T. J. McCarthy, The “Lotus Effect” Explained: Two Reasons Why Two Length Scales of Topography Are Important, *Langmuir* 22 (7) (2006) 2966–2967.
- [48] M. Sanjosé, J. M. Senoner, F. Jaegle, B. Cuenot, S. Moreau, T. Poinsot, Fuel injection model for Euler-Euler and Euler-Lagrange large-eddy simulations of an evaporating spray inside an aeronautical combustor, *Int. J. Multiph. Flow* 37 (5) (2011) 514–529.
- [49] A.-J.-C. B. de Saint-Venant, Théorie du mouvement non permanent des eaux, avec application aux crues des rivières et à l’introduction des marées dans leur lit, *Comptes Rendus des séances de l’Académie des sciences* 73 (1871) 147–154.
- [50] F. Jaegle, Large Eddy Simulation of evaporating sprays in complex geometries using Eulerian and Lagrangian methods, INPT, 2009.
- [51] P. J. O’Rourke, A. A. Amsden, A Particle Numerical Model for Wall Film Dynamics in Port-Injected Engines, *SAE Trans.* 105 (1996) 2000–2013.
- [52] G. Chaussonnet, Modeling of liquid film and breakup phenomena in large-eddy simulations of aeroengines fueled by airblast atomizers, Ph.D. thesis, École Doctorale Mécanique, Énergétique, Génie civil et Procédés, Toulouse (2014).
- [53] G. Chaussonnet, O. Vermorel, E. Riber, B. Cuenot, A new phenomenological model to predict drop size distribution in large-eddy simulations of airblast atomizers, *Int. J. Multiph. Flow* 80 (2016) 29–42.
- [54] F. Nicoud, T. Poinsot, Thermoacoustic instabilities: Should the Rayleigh criterion be extended to include entropy changes?, *Combust. Flame* 142 (1-2) (2005) 153–159.
- [55] F. Nicoud, L. Benoit, C. Sensiau, T. Poinsot, Acoustic modes in combustors with complex impedances and multidimensional active flames, *AIAA Journal*, American Institute of Aeronautics and Astronautics 45 (2) (2007) 426–441.
- [56] D. Laera, K. Prieur, D. Durox, T. Schuller, S. M. Camporeale, S. Candel, Impact of Heat Release Distribution on the Spinning Modes of an

- Annular Combustor With Multiple Matrix Burners, *J. Eng. Gas Turb. Power* 139 (5) (2017) 051505.
- [57] H. Levine, J. Schwinger, On the radiation of sound from an unflanged circular pipe, *Phys. Rev.* 73 (1948) 383–406.
 - [58] A. Ghani, T. Steinbacher, A. Albayrak, W. Polifke, Intrinsic thermoacoustic feedback loop in turbulent spray flames, *Combust. Flame* 205 (2019) 22–32.
 - [59] A. Orchini, C. F. Silva, G. A. Mensah, J. P. Moeck, Thermoacoustic modes of intrinsic and acoustic origin and their interplay with exceptional points, *Combust. Flame* 211 (2020) 83–95.
 - [60] P. G. Saffman, On the settling speed of free and fixed suspensions, *Stud. Appl. Math.* 52 (2) (1973) 115–127.
 - [61] W. A. Sirignano, C. F. Edwards, Fluid dynamics and transport of droplets and sprays, *J. Fluids Eng.* 122 (1) (2000) 189–190.
 - [62] K. K. Kuo, *Principles of combustion*, Wiley, 2005.
 - [63] G. Hubbard, V. Denny, A. Mills, Droplet evaporation: Effects of transients and variable properties, *Int. J. Heat Mass Transf.* 18 (9) (1975) 1003–1008. doi:10.1016/0017-9310(75)90217-3.